ELSEVIER

Contents lists available at ScienceDirect

Deep-Sea Research Part II

journal homepage: www.elsevier.com/locate/dsr2





Temperature variations in the northern Gulf of Alaska across synoptic to century-long time scales

Seth L. Danielson^{a,*}, Tyler D. Hennon^a, Daniel H. Monson^b, Robert M. Suryan^c, Rob W. Campbell^d, Steven J. Baird^e, Kristine Holderied^f, Thomas J. Weingartner^a

- ^a College of Fisheries and Ocean Sciences, University of Alaska Fairbanks, Fairbanks, AK, 99775, USA
- ^b US Geological Survey, Alaska Science Center, Anchorage, AK, 99508, USA
- c Auke Bay Laboratories, Alaska Fisheries Science Center, National Oceanographic and Atmospheric Administration, Juneau, AK, 99801, USA
- ^d Prince William Sound Science Center, Cordova, AK, 99574, USA
- e Kachemak Bay National Estuarine Research Reserve, Alaska Center for Conservation Science, University of Alaska Anchorage, Homer, AK, 99603, USA
- f Kasitsna Bay Laboratory, National Centers for Coastal Ocean Science, National Oceanic and Atmospheric Administration, Homer, AK, 99603, USA

ARTICLE INFO

Keywords: Gulf of Alaska Marine heatwave Temperature Warming trend GAK1

ABSTRACT

Surface and subsurface moored buoy, ship-based, remotely sensed, and reanalysis datasets are used to investigate thermal variability of northern Gulf of Alaska (NGA) nearshore, coastal, and offshore waters over synoptic to century-long time scales. NGA sea surface temperature (SST) showed a larger positive trend of 0.22 ± 0.10 °C per decade over 1970–2021 compared to $0.10\pm0.03~^\circ\text{C}$ per decade over 1900–2021. Over synoptic time scales, SST covariance between two stations is small (<10%) when separation exceeds 100 km, while stations separated by 500 km retain 50% of their co-variability for seasonal and longer fluctuations. Relative to in situ sensor data, remotely sensed SST data has limited accuracy in some NGA settings, capturing 60-70% of the daily SST anomaly in coastal and offshore waters, but often <25% nearshore. North Pacific and NGA leading modes of SST variability leave 25-50% of monthly variance unresolved. Analysis of the 2014-2016 Pacific marine heatwave shows that NGA coastal surface temperatures warmed contemporaneously with offshore waters through 2013, but deep inner shelf waters (200-250 m) exhibited delayed warming. Offshore surface waters cooled from 2014 to 2016, while shelf waters continued to warm from the combined effects of local air-sea and advective heat fluxes. We find that annually averaged Sitka air temperature is a leading predictor ($m r^2=0.37,\,p<0.05$) for following-year NGA coastal water column temperature. Our results can inform future environmental monitoring designs, assist forward-looking projections of marine conditions, and show the importance of in situ measurements for nearshore studies that require knowledge of thermal conditions over time scales of days and weeks.

1. Introduction

Northern Gulf of Alaska (NGA) marine waters (Fig. 1) provide and regulate a myriad of socioeconomic and ecosystem services, including culturally and economically important fisheries harvests, tourism, shipping, habitat for seabirds and marine mammals, and the translation and transformation of physical and biogeochemical constituents of the marine carbon pump (Mundy, 2005). The functioning and structure of these services depend on the regional geomorphology and the physical drivers that maintain the system within the climatic bounds of the sub-Arctic North Pacific. Climate change is driving this system beyond previously observed limits (Litzow et al., 2020), with spatially broad and

temporally extended temperature anomalies such as the Pacific Marine Heatwave (PMH) of 2014–2016 (Bond et al., 2015; Walsh et al., 2018).

Using more than 100 *in situ* and remotely sensed temperature datasets, this paper assesses NGA thermal variability across synoptic, seasonal and interannual time scales. Our goal is to better understand alternating intervals of cold and warm conditions (including PMH events) in the context of changing climate and regional variability. Climate models predict that marine heatwaves will increase in frequency and magnitude (Joh and Di Lorenzo, 2017; Oliver et al., 2018) and it is important to understand how these events may affect NGA biological communities. Among other consequences, warm conditions have been linked to year-class strength of commercial fish stocks

E-mail address: sldanielson@alaska.edu (S.L. Danielson).

^{*} Corresponding author.

(Hollowed et al., 2001), ecosystem regime (Anderson and Piatt, 1999) and structure (Suryan et al., 2021) shifts, and a decline in humpback whale productivity (Gabriele et al., 2022).

The NGA geomorphology includes island archipelagos, glacially carved fjord systems and subsea relict moraines and canyons, all of which impact oceanic communication between offshore and coastal waters. The bathymetric variations and basin geometry (Figs. 1 and 2) exert defining control on the Gulf of Alaska's flow field, which is important for the lateral advection of heat (Janout et al., 2013), fresh water (Royer, 1982) and biota (Weingartner et al., 2002). The steep and high-elevation (2000–6000 m) mountains rimming the Gulf of Alaska induce precipitation and route freshwater runoff into the ocean (Hill et al., 2015).

Cyclonic wind stress associated with Aleutian Low storms forces downwelling over the shelf (Royer and Emery, 1987) and upwelling within the Gulf of Alaska sub-Arctic gyre (Muench et al., 1978; Wilson and Overland, 1987; Macklin et al., 1990; Ladd et al., 2016). The gyre system includes the relatively sluggish and broad Alaska Current that flows along the Gulf's eastern boundary and the narrower and swifter Alaskan Stream that flows along the western boundary (Fig. 1). These currents advect heat from lower latitudes along the continental slope. Shelf-basin exchanges occur along the slope in association with canyons, eddies and wind-driven flows (Okkonen et al., 2003; Ladd et al., 2005, 2016; Janout et al., 2009). Aleutian Low storm systems also carry moist and warm marine air to the coastal mountain range, delivering rain or snow precipitation. Resulting coastal runoff feeds the Alaska Coastal Current (ACC; Fig. 1), which advectively connects the coastal waters of the Gulf of Alaska (Royer, 1982; Stabeno et al., 2004; Weingartner et al., 2005; Stabeno et al., 2016) and Bering Sea (Aagaard et al., 2006). For the Gulf of Alaska drainage basin as a whole, approximately 750 km³ yr⁻¹ of runoff is delivered to the inner shelf (Royer, 1982; Hill et al., 2015; Beamer et al., 2016), with the majority of the discharge occurring between April and October.

Coastal freshwater runoff and surface heat fluxes from the atmosphere into the ocean represent positive oceanic buoyancy inputs that stratify the marine water column, while ocean-to-atmosphere heat fluxes and mixing by winds and currents break down the stratification. Water column stratification depends on buoyancy inputs and the destratifying effects of mixing (Janout et al., 2010) that develop over storm cycles and seasons. The summer NGA water column is typically characterized by relatively strong near-surface stratification, often near 15–20 m depth. Lateral advection both at the surface and at depth also

contribute to the heat and haline balances and water column structure (Weingartner et al., 2005).

In addition to the synoptic variability of Aleutian Low storms, the NGA is subject to hemispheric-scale modes of climate variability, including the Pacific Decadal Oscillation (PDO; Mantua et al., 1997), the North Pacific Gyre Oscillation (NPGO; Di Lorenzo et al., 2008) and the El Niño Southern Oscillation (ENSO; Cane and Zebiak. 1985). Atmospheric teleconnections can reinforce and transmit the influence of climate signals across broad latitudinal and longitudinal extents (e.g. Chiang and Vimont, 2004) with time scales corresponding to the structure, size and propagation characteristics of the oceanic and atmospheric processes and interactions.

A record-breaking PMH (Hobday et al., 2018) developed in the Northeast Pacific during late 2013 (Bond et al., 2015) because of a persistent atmospheric high-pressure ridge that inhibited winter storm mixing in the region (Swain, 2015). Spatially nonuniform warming continued through 2014 and intensified as strong El Niño conditions developed in 2015–2016 (Di Lorenzo and Mantua, 2016). The PMH was particularly unusual in duration and magnitude (Hobday et al., 2018), with massively large positive temperature anomalies, and unusual warming down to 300 m depth in the basin and throughout the entire water column over the shelf (Jackson et al., 2018). Mixed layer heat budget analyses identified resulting anomalies in atmospheric and oceanic processes and conditions that together caused the anomalously warm sea surface temperatures (SSTs) to persist for at least two years (Schmeisser et al., 2019); over-winter mixed layer re-emergence mechanisms may have played a role (Alexander et al., 1999).

This manuscript assesses NGA thermal variability, with the benefit of now decades worth of modern oceanographic observations, in order to form a more integrated understanding of this region's ecologically important thermal structure and temporal evolution. Following an overview of the data types and analytical methods (Section 2), we examine long-term (decades to centuries) temperature trends and interannual co-variability (Section 3.1), and large spatial scale thermal structure (3.2). We then place the spatial analyses that rely on remote sensing into a more complete context by assessing satellite data fidelity across the study region (3.3). Station data allow us to examine horizontal and vertical scales of variability (3.4), and temporal co-variability across the coastal and nearshore zones (3.5). Finally, we assess the spatio-temporal evolution of the 2014–2016 NGA PMH (3.6) and then provide concluding discussion and summary statements (Section 4).

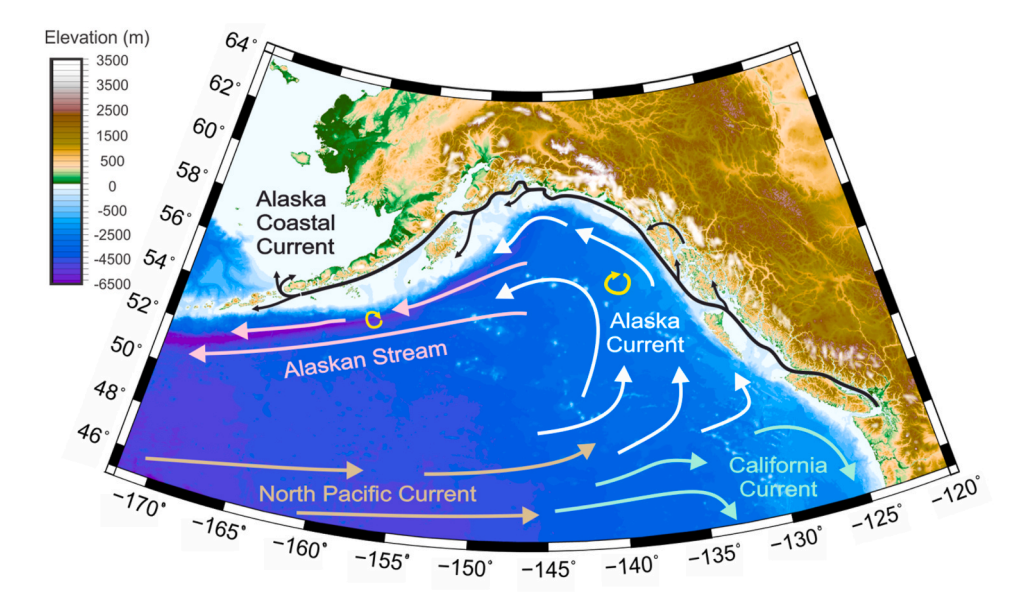


Fig. 1. Ocean circulation, land topography and ocean bathymetry in the Gulf of Alaska.

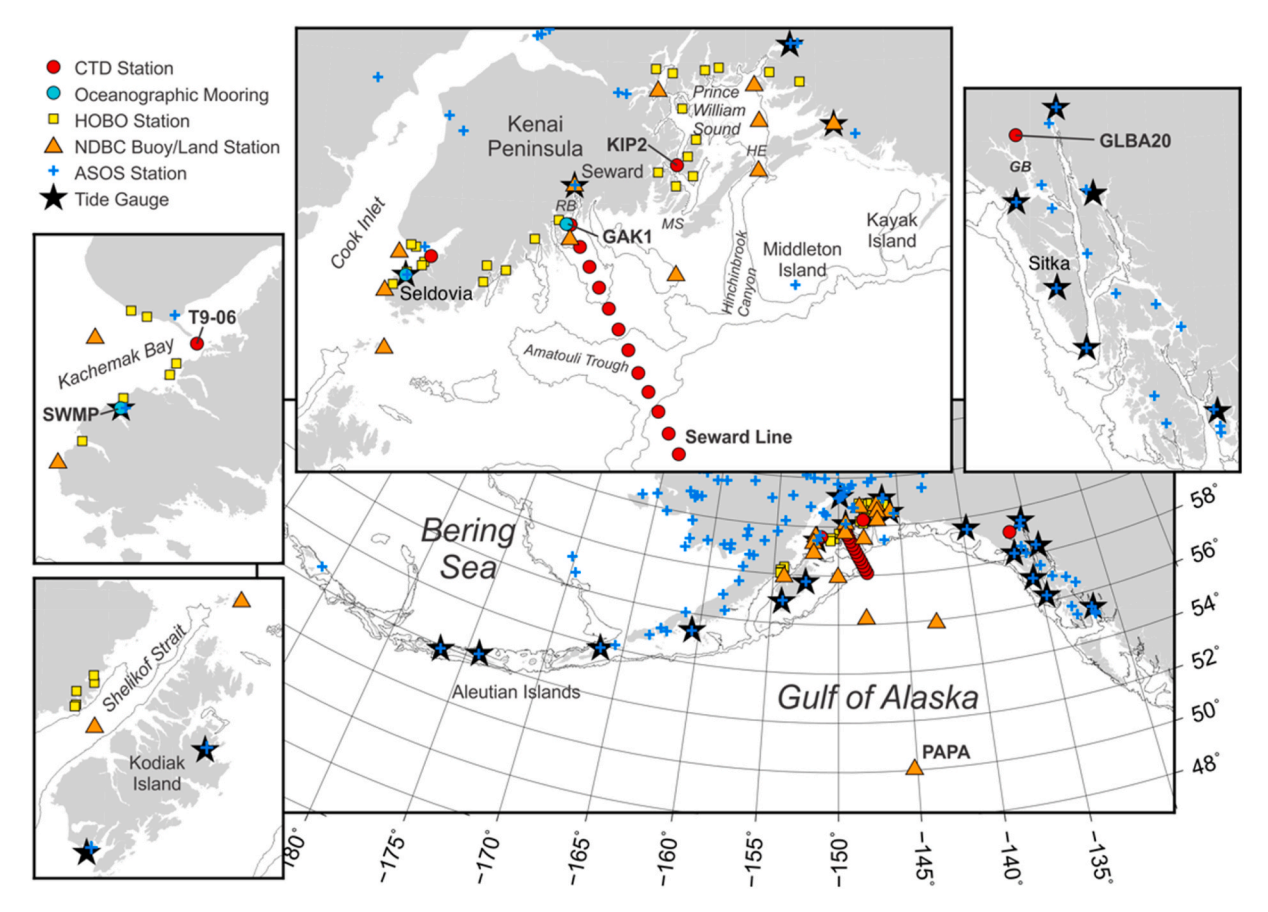


Fig. 2. Study region maps showing place names and station locations, including GAK1 and System Wide Monitoring Program (SWMP) moorings (cyan circles), buoys and land stations (orange triangles), tide gauge stations (black stars), weather stations (blue plus symbols), intertidal HOBO data loggers (yellow squares), and conductivity-temperature-depth stations (red circles). See Table S1 for station coordinates, data temporal coverage and site characteristics. Abbreviations include: RB = Resurrection Bay; GB = Glacier Bay; HE = Hinchinbrook Entrance; MS = Montague Strait. Bathymetric contours are drawn at 180 and 1000 m depths.

2. Data and methods

Herein we analyze a variety of $in \, situ$ and remotely sensed oceanic temperature data, weather station data, reanalysis model output, and climate indices.

Our datasets span nearshore, coastal, shelf and offshore waters. We distinguish between these regions based on their contrasting characteristics and functional dynamics. Nearshore waters, a subset of coastal waters lying immediately adjacent to land, include the intertidal zone and subtidal waters where the proximity of these sites to land extensively alters water column chemistry, biological communities, physical habitat, and physical dynamics relative to the coastal shelf waters. The nearshore zone is often an energetically active environment under the influence of surface waves and swell, where effects of sunlight illumination reaches the seafloor, the relative importance of cross-shelf wind forcing often dominates over along-shelf winds, along-shore tidal currents dominate over cross-shore tidal currents, and the surface and seafloor boundary layers tend to overlap (Fewings et al., 2008).

Shelf waters encompass coastal waters and waters inshore of the continental shelf break. Coastal waters comprise the riverine coastal domain (Carmack et al., 2015), which occupies the inner portion of the continental shelf and is strongly under the influence of terrestrial freshwater discharge. For the NGA, the Alaska Coastal Current (ACC) salinity front defines the coastal domain mid-shelf boundary, commonly found 25–35 km from the coast in non-summer months (Weingartner et al., 2005). Outer shelf waters lie between coastal waters and the shelf break. Offshore, or oceanic waters, lie beyond the shelf break over the continental slope and deep basin.

Ocean temperature data were assembled from moored buoys, ship-

based water column conductivity-temperature-depth (CTD) instrument profiles, and data loggers fixed within the intertidal zone (Table 1 and Fig. 2). A detailed description of data collection and handling of *in situ* oceanic temperature measurements is provided in the supplementary materials text, along with site locations and characteristics.

Different SST measurement techniques impart cross-platform differences in this parameter's measurement. For example, satellites that measure the surface radiative heat report the "skin temperature" associated with the thin molecular layer at the very surface, while ship-based CTD data are typically averaged into 1 m thick layers. CTD dimensions and mixing associated with a vessel's propellers may only allow a CTD cast to resolve the surface temperature as a blended average of the uppermost few meters of the water column. Sensors affixed to the seafloor in the nearshore environment constantly change depth relative to the sea surface due to waves, storm surges, and tides. A buoy floating at the surface will often have an SST sensor maintained at a fixed depth (typically 1 m) below the surface. Despite such cross-platform differences, in order to compile the largest surface temperature dataset possible and because we focus our analyses on anomalies that minimize systematic bias, we consider each of these measurement types to provide comparable SST data.

2.1. Intertidal dataloggers

We deployed HOBO water temperature loggers (Onset Computer Corporation, Bourne, MA USA) at 28 intertidal sites distributed among six focal areas in the NGA: Eastern PWS (EPWS), Northern PWS (NPWS), Western PWS (WPWS), Kenai Fjords National Park (KEFJ), Kachemak Bay (KBAY) and Katmai National Park and Preserve (KATM; Fig. 2 and

Table 1In situ, remotely sensed, and reanalysis data types and sources used in the analyses herein.

Dataset	Data Type	Source
Intertidal Dataloggers	in situ temperature HOBO dataloggers	https://gulfwatchalaska.
Tide gauge stations	in situ temperature datalogger	https://tidesandcurrents. noaa.gov/
GAK1 and Seward Line hydrography	in situ moored fixed depth CTD dataloggers and shipboard CTD profiles	https://search.dataone. org/portals/NGALTER
Kachemak Bay National Estuarine Research Reserve hydrography	in situ moored fixed depth CTD dataloggers and shipboard CTD profiles	http://cdmo.baruch.sc. edu/
Glacier Bay hydrography	in situ shipboard CTD profiles	https://www.nps. gov/im/sean/oceanograph y.htm
Weather stations	in situ land-based and buoy-based weather data	https://www.ndbc.noaa. gov/
Automated Surface Observing System (ASOS)	in situ land-based weather data	https://mesonet.agron. iastate.edu/ASOS/
Group for High Resolution Sea Surface Temperature (GHRSST)	Remotely sensed satellite SST	https://podaac.jpl.nasa. gov/dataset/MUR-JPL-L4- GLOB-v4.1
Optimum Interpolation SST (OISST)	Blended product: satellite, buoy and ship data	https://www.ncdc.noaa. gov/oisst
Extended Reconstructed SST (ERSST)	Blended product: satellite, buoy and ship data	https://www.ncdc.noaa. gov/data-access/marine ocean-data/extended-re constructed-sea-surface-te mperature-ersst-v5
Atmospheric Model Inter- comparison Project-II Reanalysis (NCEP-R2)	Reanalysis	http://www.cpc.ncep.noaa .gov/products/wesley/rea nalysis2/

Appendix Table S1). HOBO sensors were placed at 0.5 m mean lower low water (MLLW) tidal elevation inside a 1.5" (3.8 cm) diameter white PVC pipe that was securely bolted to a boulder or bedrock.

We determined the fraction of time each logger was submerged each day (Appendix Table S1) and explored different methods to estimate daily averages from these incomplete records. These different techniques yielded little quantitative difference in analysis, and the magnitude of the distorted signal is small relative to the magnitude of thermal fluctuations of primary interest. Daily averages reported here were computed from only the submerged measurements.

2.2. Marine weather station, tide gauge and buoy data

We downloaded records from the National Oceanic and Atmospheric Administration's (NOAA's) National Data Buoy Center (Table 1) for 16 land-based stations and moored buoys spanning both coastal and offshore realms (Table S1). Temperature data from 18 tide gauge stations were obtained from the NOAA Center for Operational Oceanographic Products website (Table 1).

2.3. Shipboard CTD data

A temperature and salinity hydrographic profile time series has been maintained on a quasi-monthly basis since December 1970 at oceanographic station GAK1, which is located at the mouth of Resurrection Bay near Seward, AK in 273 m of water (Fig. 2). GAK1 is the innermost station of the Seward Line hydrographic transect, which was occupied 103 times from 1974 to 2021.

Since 1993, CTD monitoring has been accomplished 4–9 times per year in the marine waters of Glacier Bay National Park and Preserve

(GLBA). Data from monitoring station GLBA20 provides a record of temperature and salinity variations close to meltwater discharges from a tidewater glacier.

Routine monthly oceanographic profiles were conducted at 10 stations along a cross-bay transect in Kachemak Bay from 2012 to present. For this paper, we used water column temperature data from the midbay station (designated T9-06) from 78 monthly surveys conducted from 2012 to 2018.

2.4. Oceanographic mooring data

We combined GAK1 CTD profile and GAK1 moored CTD data into two time series: an aggregate monthly mean vertical profile time series spanning the 1970–2021 GAK1 period of record, and a daily profile time series spanning only the 2000–2019 period of GAK1 mooring deployments.

A CTD datalogger was also continuously deployed on a mooring near the Seldovia ferry dock in Kachemak Bay since August 2001, at 59.44097 $^{\circ}$ N, 151.72089 $^{\circ}$ W, as part of Kachemak Bay National Estuarine Research Reserve's System Wide Monitoring Program (SWMP). The logger is deployed 1 m above the seafloor at a depth of \sim 8 m.

2.5. Gridded SST compilations

We used three satellite-based SST datasets to assess the spatial structure of NGA thermal variations and to assess the validity of the satellite-based sensors in this notoriously cloudy region.

The Group for High Resolution Sea Surface Temperature (GHRSST) Level 4 product is a high-resolution (daily time step, 0.01° spatial grid) surface temperature compilation, using data from multiple satellites (Chin et al., 2017). We extracted data from GHRSST at the grid points closest to the fixed intertidal datalogger, mooring and hydrographic stations

NOAA's Earth System Research Lab compiles a blended medium-resolution (1981-present daily time step, 0.25° spatial grid) SST data-set from available Advanced Very High Resolution Radiometer satellite, ship and buoy data into the Optimum Interpolation SST (OISST) dataset (Reynolds et al., 2007).

NOAA also compiles a blended low-resolution long-term (1854-present, monthly time step, 2° spatial grid) SST from available ship, satellite and buoy data (Huang et al., 2017) as the Extended Reconstructed SST (ERSST) dataset, version 5.

2.6. Meteorological station data

The Iowa Environmental Mesonet at Iowa State University maintains an archive of Automated Surface Observing System (ASOS) meteorological data, including records from 185 Alaskan land-based stations. We downloaded air temperature, dew point temperature, relative humidity, wind speed and direction, sea level pressure, and sky cover data from January 2000 to October 2019 for all Alaska region stations.

The longwave loss (Q_{LW}) from the ocean was estimated using daily averages of SST from the closest oceanographic station, assuming blackbody radiation ($Q_{LW} = \varepsilon \sigma T^4$ where the emissivity $\varepsilon = 0.98$ and the Stefan-Boltzman constant $\sigma = 5.7 \times 10^{-8}$ J s⁻¹ m² K⁻¹). The downward longwave radiation was defined as backscatter (Q_{BS}) reflected into the ocean from the cloud cover (CC) with modified emissivity $\varepsilon = 0.78(1 + 0.22CC^{2.75})$ and air temperature. Estimates of surface latent heat flux (Q_{LA}) used the relative humidity, latent heat of evaporation and wind speed from the weather station and assume 100% saturation at the surface of the ocean. The sensible heat flux (Q_{SE}) was derived from wind speed and the difference between SST and air temperature at the weather station. Shortwave radiation surface heat flux (Q_{SW}) estimates were based on 6-h averages of clear-sky downward radiation from the NCEP-R2 and an assumed ocean albedo of 0.2. The total surface heat flux estimate Q_{SUM} using the bulk formulae is the combination of the

shortwave, longwave, sensible and latent terms.

ASOS data were also used to update a now 193-year air temperature time series (Royer, 1989, 1993) from Sitka, Alaska (Royer, pers. comm.). Corrections (Wendler et al., 2016) were previously applied for unit conversions and station relocations, including a 0.9 $^{\circ}$ C offset for measurements made at the nearby historic observation site relative to contemporary measurements made at the Sitka airport. We did not apply any adjustment to account for partial-day measurement schedules for observations taken before 1848, which if applied would have the effect of decreasing the annual anomalies in this time frame by about 0.3–0.5 $^{\circ}$ C (Wendler et al., 2016).

2.7. Atmospheric reanalysis

We obtained monthly mean surface heat flux estimates from the NOAA Earth System Research Laboratory Physical Sciences Division, National Centers for Environmental Prediction-Department of Energy, Atmospheric Model Intercomparison Project-II Reanalysis (NCEP-R2) (Table 1) for 2010–2015. The NCEP-R2 model is computed on a 208 km global grid, but this resolution is sufficient to reveal broad-scale ocean-atmosphere heat exchange patterns across the North Pacific.

Downloaded model variables include the downward (Q_{DSW}) and upward (Q_{USW}) shortwave radiation heat flux, the downward (Q_{DLW}) and upward (Q_{ULW}) longwave radiation heat flux, the sensible heat flux (Q_{SE}) and the latent heat flux (Q_{LA}). The individual surface heat fluxes terms were combined to form the net surface heat flux $Q_{NET} = Q_{DLW} + Q_{DSW} - Q_{ULW} - Q_{USW} - Q_{E} - Q_{LA}$, using the convention that positive heat flux represents a gain of heat by the ocean from the atmosphere. Although NCEP-R2 model heat fluxes have known biases in the NE Pacific (Ladd and Bond, 2002), by evaluating monthly anomalies relative to the annual climatology we were able to assess relative changes in the heat flux forcing and the anomalies should be relatively insensitive to any residual bias.

2.8. Climate indices

Time series of large-scale climate patterns were used to help diagnose the source of local NGA SST fluctuations; these were downloaded from the sources given in Table 2.

2.9. Temperature analyses

We defined synoptic-scale variability to be fluctuations for periods spanning $1{\text -}30$ days. Seasonal to interannual (low-frequency) variability occurs at time scales longer than 30 days; analyses of the low-frequency signals were often best accomplished using daily or monthly anomalies

Table 2Indices of climate variability in the Pacific region. Table columns include index name, abbreviation, and data source.

Index Name	Abbreviation	Source
Pacific Decadal Oscillation	PDO	http://jisao.washington. edu/pdo/PDO.latest
North Pacific Gyre Oscillation	NPGO	http://www.o3d.org/npgo/npgo. php
Multivariate ENSO (El Niño Southern Oscillation) Index version 2	MEI	https://www.esrl.noaa.gov/psd /enso/mei
Pacific North American Index	PNA	https://www.cpc.ncep.noaa.gov/data/teledoc/pna.shtml
Pacific Meridional Mode	PMM	https://www.esrl.noaa.gov/psd /data/timeseries/monthly/PMM/
North Pacific Index	NPI	https://climatedataguide.ucar.edu /climate-data/north-pacific-np-i ndex-trenberth-and-hurrell- monthly-and-winter
Victoria Mode Index	VMI	Computed with the ERSST grid following Ding et al. (2015)

in which the annual climatology is removed.

Monthly anomaly time series were generated by subtracting the climatological monthly mean from each corresponding monthly average to create an anomaly that retains units of °C. Daily and seasonal anomalies were constructed in a parallel fashion, but using a daily or seasonal climatological mean and standard deviation rather than the monthly climatology. Some operations required normalized anomalies, for which each individual monthly anomaly was divided by the standard deviation for the corresponding set of monthly means, resulting in a record having zero mean and unity variance. Some analyses required normalization of a record relative to a reference station; such instances are noted where they occur.

Frequency band evaluations (Fig. 3) separately consider three components of variation: the annual cycle based on smoothed climatological day-of-year average, or "daily climatology" (T_{DC}); synoptic-scale fluctuations of less than 30 days were formed by high-pass filtering the daily anomalies (T_{HP}), where daily anomalies were computed by subtracting T_{DC} from the raw temperature record; the remaining low frequency variations encompass both seasonal and interannual variability and were formed by low-pass filtering the daily anomalies (T_{LP}). To ensure minimal filter-induced distortion, the frequency separation was based on a 6th order phase-preserving band-pass Butterworth filter applied to the daily averaged records.

To assess the statistical strength and significance of covariation, we computed the standard deviation (σ), root-mean-square-difference (RMSD), Spearman's cross-correlation (r) and p-value parameters. Statistical significance was ascribed only for p < 0.05. Slope detrending was based on least-squares fits. The first zero crossing of the autocorrelation function provided a measure of decorrelation time scales. Empirical orthogonal function (EOF) analysis was used to identify linked spatial and temporal patterns of variability. We computed an EOF decomposition of the gridded ERSST and OISST datasets using standard normalized (unity variance and zero mean) and detrended monthly anomalies. We applied stepwise multivariate regressions (Harrell, 2001) to assess the correspondence between large-scale climate patterns and local temperature fluctuations.

3. Results

3.1. Climate context

For the period when the GAK1, Sitka and ERSST records overlap (1970-2021), these time series exhibit correspondence in the relative magnitude and sign of their annual temperature anomalies, showing that the Gulf-wide average SST during strong and prolonged warm and cool events generally varies in phase with the air temperature and the depth-mean temperatures on the northern inner shelf (Fig. 5). The Gulfwide SST record of annual anomalies since the start of the 20th century exhibits a linear warming trend (p < 0.001) of 0.10 \pm 0.03 °C decade⁻¹ from 1900 to 2021. The trend explains 25% of the total annually averaged SST variance over this time period. For 1970-2021 we find a warming trend (p < 0.001) of 0.22 \pm 0.10 $^{\circ} C \; decade^{-1}$ for the coastal northern shelf at oceanographic station GAK1 (0-250 m depth average) and an identical Gulf-wide SST trend of 0.22 \pm 0.10 $^{\circ}$ C decade⁻¹. The Sitka annual air temperature trend is 0.050 \pm 0.03, 0.078 \pm 0.04, and 0.21 ± 0.14 °C decade⁻¹ for the 1828–2021, 1900–2021, and 1970-2021 time intervals, respectively. The Gulf-wide annual average SST since the start of the recent PMH (2014-2021) has been 1.20 °C above the long-term mean, 2.03 °C warmer than the first decade of the 1900s, and 2.19 $^{\circ}\text{C}$ warmer than the mean of 1970–1976.

A climate shift in 1976 impacted much of the North Pacific (Hare and Mantua, 2000; Litzow and Mueter, 2014) and was associated with far-reaching biological and economic consequences as this warming played an important role in the restructuring of the NGA marine ecosystem and its fisheries (Anderson and Piatt, 1999). Debate persists over appropriate terminology and designation of climate and ecological

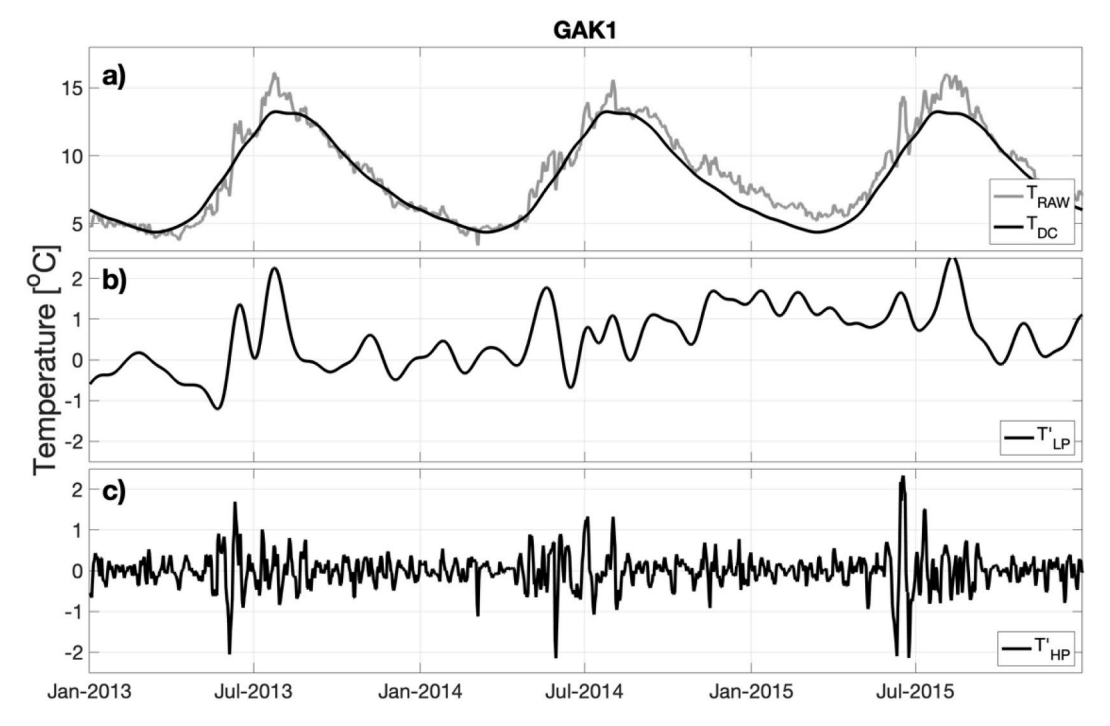


Fig. 3. Three-year example of sea surface temperature (SST) at GAK1 decomposed into different periods of variability using 6th order zero phase-shift Butterworth filters. a) Raw SST at GAK1 (T_{RAW}) and the climatological average SST for each day of year (T_{DC}). T_{DC} is low-pass filtered with a cutoff period of 60 days. b) The daily anomaly (T_{RAW} - T_{DC}) low-pass filtered with 30-day cutoff period (T_{LP}). c) The daily anomaly high-pass filtered with a 30-day cutoff period (T_{LP}). The entire record (over which T_{DC} , T_{LP} , and T_{LP} are calculated) spans January 2007 to May 2018.

regime shifts (Overland et al., 2008) but regardless of the definition, we found that 1976 still stands out as singularly notable transition within the long-term record (Fig. 4).

Correlation analysis amongst Fig. 4 time series (detrended) shows that the Sitka air temperature record is a weak but significant predictor of the following-year SST ($r=0.19,\,p<0.05$ for 1898–2021). Over

1970–2021, GAK1 water column mean temperature anomalies are related to the prior year Sitka air temperature (r=0.49, p<0.05; Fig. 5) and the prior year Gulf-wide SST (r=0.41, p<0.05) anomalies. The GAK1 record autocorrelation at a lag of 1 is r=0.53 without detrending and r=0.35 with detrending. Using not-detrended records, the GAK1 vs. Sitka and ERSST correlation coefficients are r=0.61 and r=0.60,

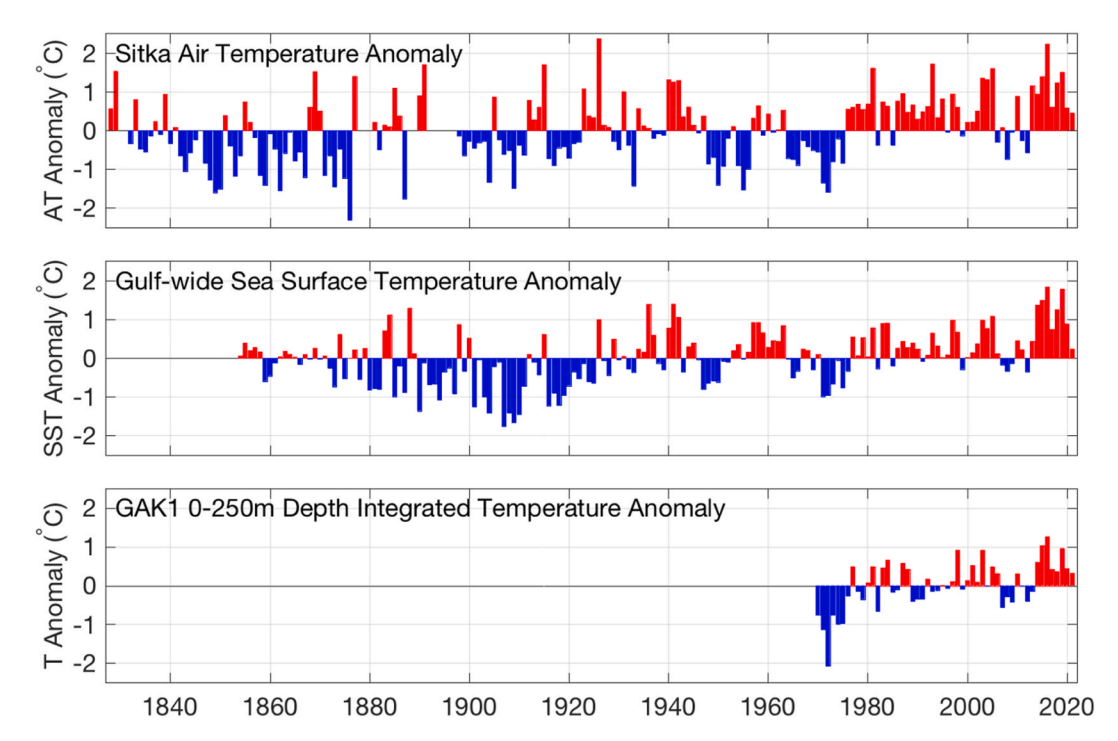


Fig. 4. Annual averages of monthly temperature anomalies (seasonal climatology removed) for three long-term datasets. Upper panel: 1828–2021 Sitka, Alaska air temperature. Middle panel: 1854–2021 ERSST V5 sea surface temperature averaged over 156° W to 130° W and 56° N to 62° N. Lower panel: 1970–2021 GAK1 water column temperature averaged across 0–250 m depths. All three records are shown relative to a 50-year baseline computed over 1970–2019.

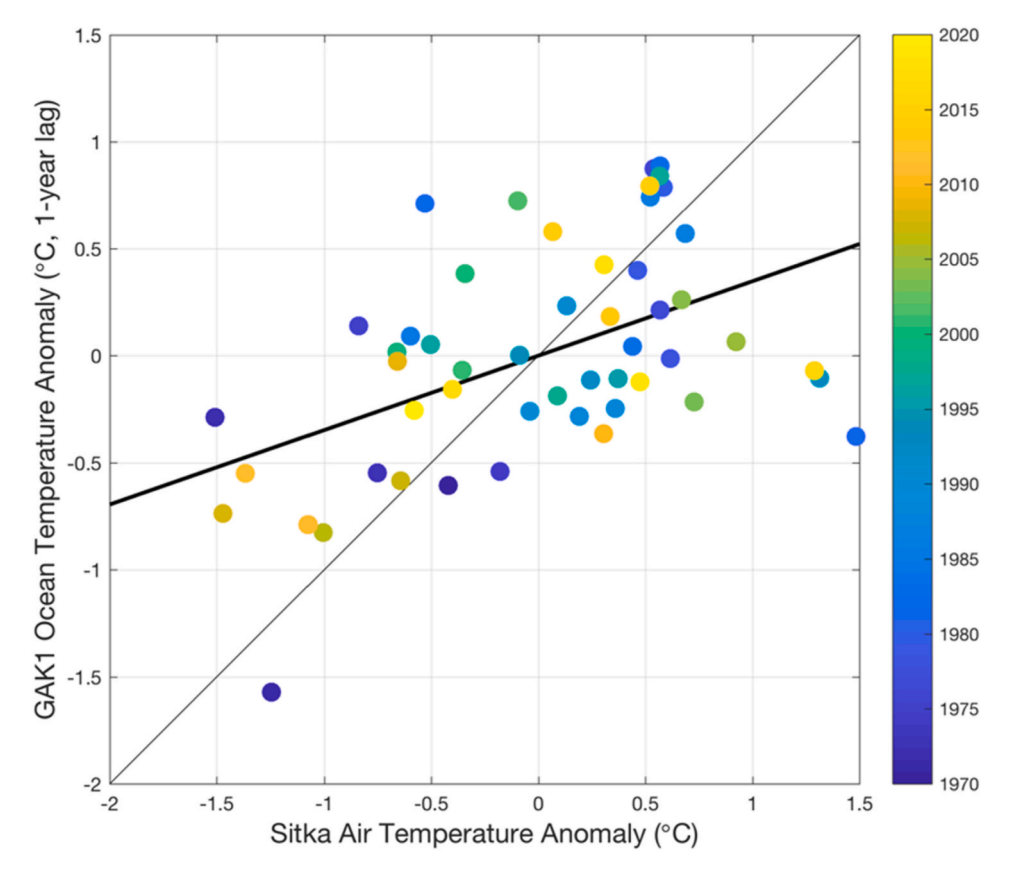


Fig. 5. Relationship between the detrended annual Sitka air temperature anomaly and the following-year whole water column ocean temperature anomaly measured at station GAK1. Thin black line shows a 1:1 slope; the thick black line is the least squares best fit line between the two records.

respectively. These relationships speak to the prolonged thermal memory in the NGA marine system, and highlights a potential utility of these records for providing forward-looking metrics of following-year marine conditions.

3.2. Large-scale patterns of temperature variation

Turning to the gridded SST fields, basin-scale signals emerge from the leading modes of SST variation using EOF analysis of the ERSST and OISST datasets (Fig. 6). The loading functions exhibit only modest magnitudes in the NGA, raising the question of their importance to local conditions in the Alaskan coastal zone where the coarsely gridded SST records are not expected to accurately represent small-scale spatial variations (e.g. the ERSST 2-degree grid vastly exceeds a typical 10 km coastal baroclinic Rossby radius of deformation). Unsurprisingly, the EOF time series for the selected analysis regions (Fig. 6b) relate closely to well-known patterns of climate variability. The PDO (Mantua et al., 1997), multivariate ENSO index version 2 (MEI; Wolter and Timlin, 2011) and Victoria mode index (VMI; Ding et al., 2015) indices (left hand columns of Fig. 6a. b) emerge from the monthly ERSST analysis. For the daily time series confined to the NGA (right hand column of Fig. 5a and b), the first three OISST EOF modes are significantly correlated to the PDO, VMI and NPGO (Di Lorenzo et al., 2008) time series (see Table S2 for correlation values).

The relation between the large-scale climate modes and the coastal Gulf of Alaska was further diagnosed using simple regression between surface layer (0–50 m average) temperature fluctuations at GAK1 and each record (Table S2). The univariate regressions show that the leading mode of variability (PDO or EOF1 of the OISST) captures $\sim 50\%$ of the GAK1 thermal anomaly. We note that coastal warming from 2012 through 2014 (discussed in detail below in Section 3.5) is captured in the time series of the PDO, ENSO and VMI time series. In particular, the VMI

signal stands out with a record maximum in 2014.

We also calculated a stepwise multiple regression between the GAK1 record and the leading modes of variability. The stepwise multivariate regression captures $\sim\!65\%$ of the total variance. The leading covariates that are included in the best stepwise models include the EOF1 and EOF3 of the OISST record, the PDO and the MEI with a 6-month lag. At the Seldovia tide gauge station (Fig. 2), the stepwise model only accounts for about 50% of the total variance, suggesting that thermal variability in the Cook Inlet nearshore zone is less closely linked to the broad-scale thermal fluctuations than those at GAK1.

We next assess zero-lag correlations of surface temperature daily anomalies across the Gulf (Fig. 7). For the reference locations shown in Fig. 7, GAK1 (Fig. 7c) is found to be the most representative of the northern shelf, with the r=0.7 contour (which accounts for $\sim 50\%$ of the variance) extending from east of Kayak Island to nearly Kodiak Island. The grid point at Sitka (Fig. 7d) is well correlated only to a narrow band of grid points that stretches along the southeast shelf, suggesting that this region is characterized by relatively small spatial scales of variability. SST variations within PWS (Fig. 7b) appear to be primarily confined to the Sound and a short advective corridor immediately downstream; Cook Inlet SSTs (Fig. 7a) behave similarly.

The regression analysis of Fig. 7 suggests that temporal thermal anomalies in the Gulf of Alaska exhibit spatial characteristics that can be ascribed to the influence of the generally counter-clockwise ocean circulation field in both coastal and slope region waters (see Fig. 1). For example, the correlation at GAK1 (Fig. 7c) is near r=0.6, and this contour extends southwest from PWS. The r=0.5 contour extends more than $100 \, \text{km}$ downstream along the coast southwest of GAK1, suggesting that temperature variations at GAK1 are more representative of those in the waters flowing by the Kenai Peninsula than they are of the variations in coastal waters located a similar distance to the east of PWS. Correlation contours over the central Gulf of Alaska are aligned primarily

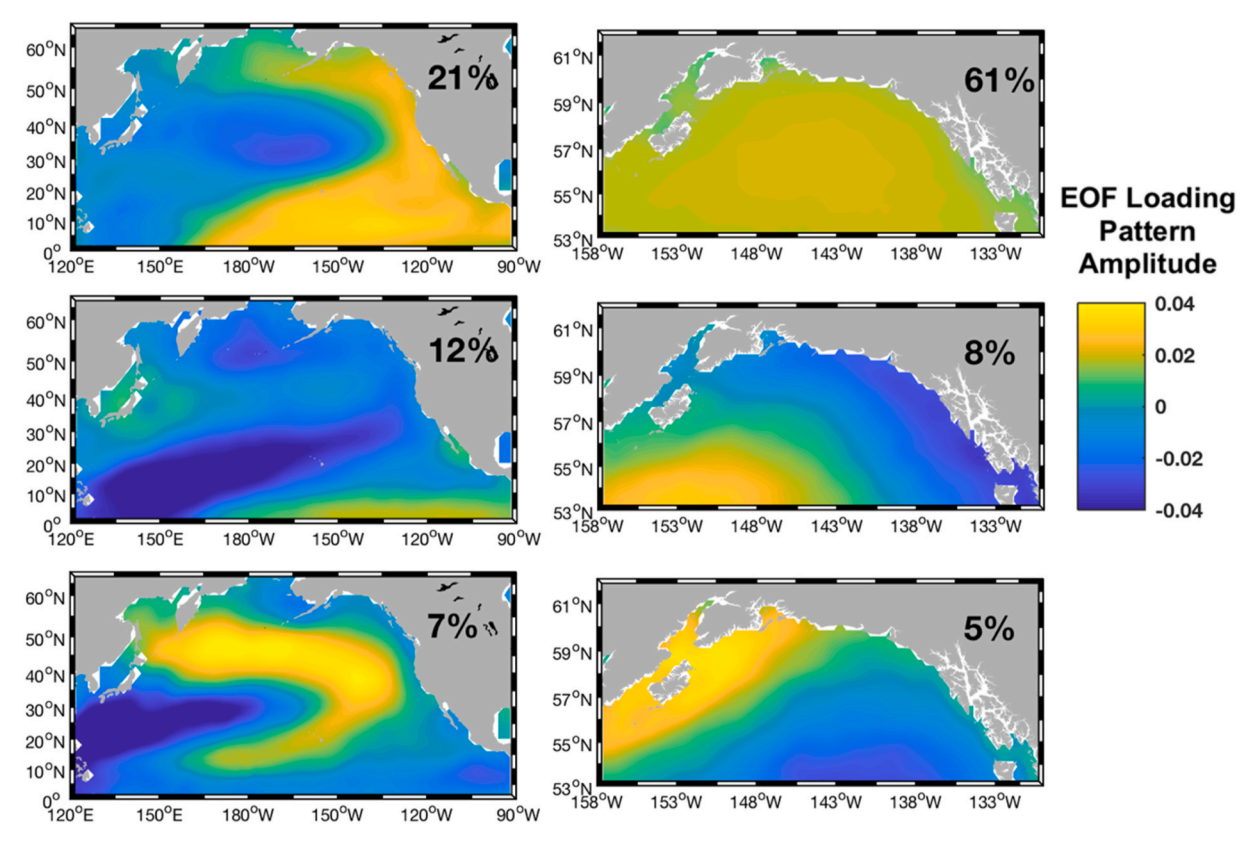


Fig. 6a. North Pacific (left) and Gulf of Alaska (right) patterns of sea surface temperature (SST) variation based on empirical orthogonal function analysis of 1900–2019 ERSST monthly anomaly records (left) and 1981–2019 OISST daily anomaly records (right). Anomaly time series at all grid points were detrended and normalized to unity variance and zero mean. Color bar scale clipped to \pm 0.04. From top to bottom, the rows represent modes 1, 2 and 3, respectively. The fraction of total variance contained in each mode is shown in the upper right-hand corner of each plot.

zonally and near the Southeast (SE) Alaska archipelago they intersect the continental slope at approximately a right angle, while in the region of the swift Alaskan Stream in the western Gulf the correlation contours are more aligned along the shelf break.

Despite the relatively coarse quarter-degree grid resolution of the OISST compilation, the correlation contours of Fig. 7 distinguish differences in coastal and offshore thermal regimes. This can be seen, for example, in anomalies connected to the coast of SE Alaska and extending to the northern coast past Kayak island, and with declining correlation over the basin. Similarly, relative to GAK1 the correlations degrade in Northern PWS and in upper Cook Inlet. The OISST product does not extend into the narrow passages of SE Alaska or PWS, so to better understand the conditions in these locations we turn to other data sources below. The results above raise the question of how well satellite products capture *in situ* temperature fluctuations, and whether the satellite data are equally reliable in the nearshore, coastal and offshore realms.

3.3. Linking remotely sensed and in situ SST data

The monthly GAK1 profile time series is based in part on mooring data and so lacks measurements between the surface and the uppermost mooring sensor in months with no ship-based CTD profiles. To extend the GAK1 temperature data across this gap, we generated a hybrid *in situ* and remotely sensed dataset compilation by using the daily OISST time series from the grid point closest to the GAK1 site. The OISST dataset is corrected using a variety of buoy and ship-based surface measurements, but not hydrographic profile data so comparisons against measurements made at GAK1 are not biased by assimilation.

Comparing surface temperatures from GAK1 CTD profiles and the OISST data from the closest grid point on the day of observation, we find an overall (annual cycle included) cross-correlation of $r=0.98,\,p<$

0.001 and a RMSD of 0.61 °C (Fig. S1). The *in situ* standard deviation (3.5 °C) is somewhat larger than that of the gridded product (3.1 °C). Correlation of 0 m depth CTD daily anomalies with OISST daily anomalies shows that the OISST dataset accounts for nearly 60% of the *in situ* daily variance (r = 0.77, p < 0.001). Corresponding analyses for the GHRSST dataset show r = 0.99, p < 0.001 and RMSD = 0.39 for the raw data and almost 70% of the daily anomaly variance (r = 0.83, p <0.001). Individual ship-based measurements of SST are known to often have a bias of a few tenths of a degree and RMSD errors on the order of 1 °C (Reynolds et al., 2007). Hence, the satellite SST data capture the annual cycle of GAK1 conditions with appreciable fidelity and they reproduce the majority of the synoptic-scale variability. However, a large fraction (30–40%) of the daily anomaly variance remains unresolved by the satellite data, with typical random errors of about ± 0.5 °C.

Comparing the OISST and GHRSST daily anomalies to those at the HOBO deployment sites, tide gauge and buoy stations, we find that the relation is strongest for the offshore stations (Fig. 8 and S3). Weak correlations (r < 0.4) exist across all the southeast Alaska stations, around the perimeter of PWS and along the Aleutian Islands. Often, these stations with low correlations are in relatively protected embayments that lack a direct connection to the shelf circulation, and are also in regions of very high precipitation and cloud cover. Remotely sensed SST measurements are often less accurate in nearshore waters because this realm often exhibits high suspended sediment loads, and turbidity affects both water surface emissivity (Wei et al., 2017) and shortwave absorption (Kara et al., 2004). Because of its smaller observation footprint, the GHRSST measurements capture a higher fraction (5-25%) of the in situ variability at some sites. The problems with the satellite data are likely most prevalent when the satellites are on their North-to-South trajectories over the NGA. In a descending orbit, by the time the sensors adjust to the water they are offshore some distance.

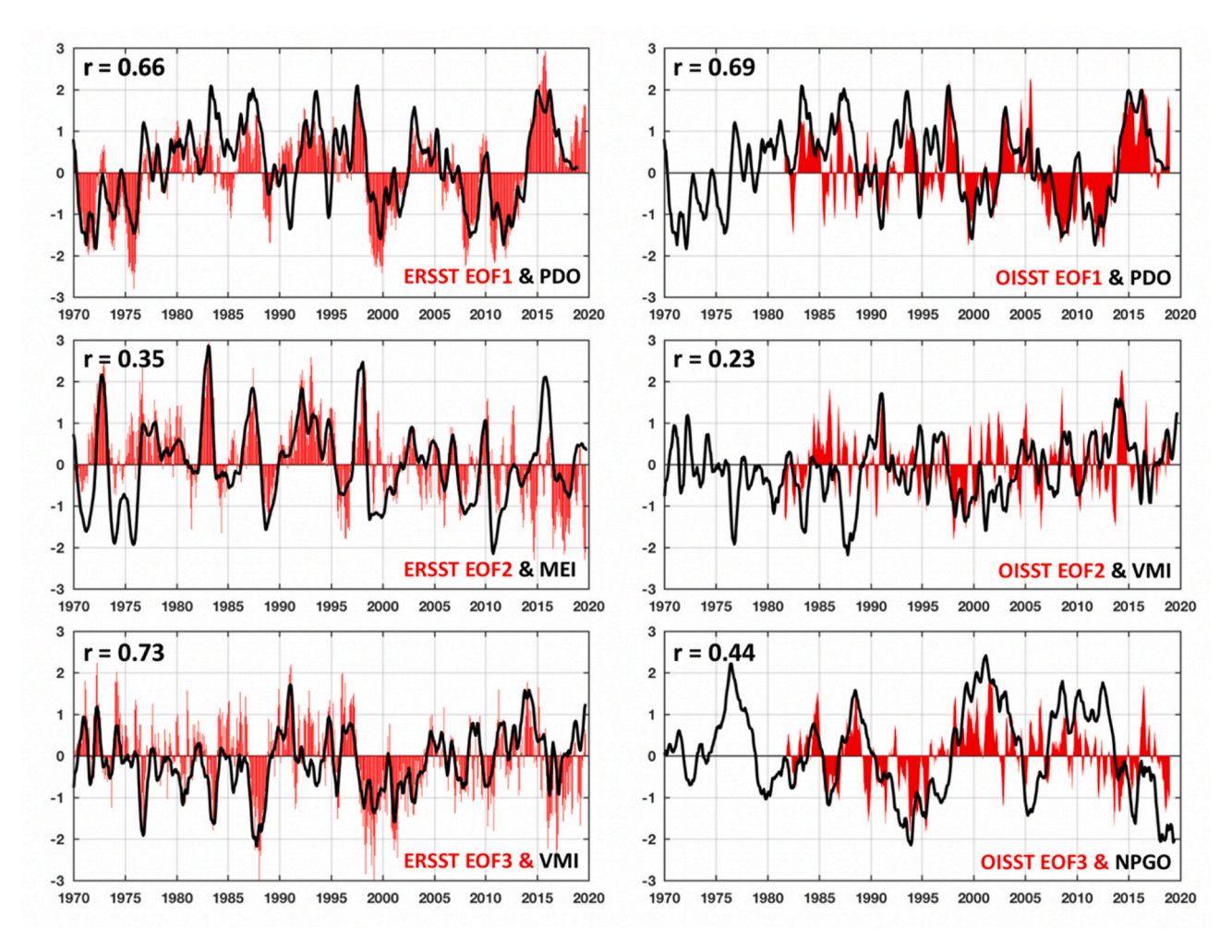


Fig. 6b. Time series (red bars) for the six modal patterns shown in Fig. 6a, along with the best-correlated climate pattern time series (see also Table S3). From top to bottom in the left column, the black lines show PDO, MEI and VMI time series, and in the right column the PDO, VMI and NPGO time series, respectively. Black lines are smoothed with a 6-month moving average filter. OISST time series have been smoothed with a 31-day moving-average filter. See Table 2 for climate index abbreviation definitions. The zero-lag correlation coefficient, r, between each record pair is denoted on each panel. All correlations are significant at p < 0.05.

In summary, we find that the higher spatial resolution GHRSST data are superior to the lower resolution OISST data in representing near-shore surface temperatures. However, the GHRSST data fail to capture the majority of the daily anomaly in the nearshore zone. Hence, the satellite products are not necessarily useful for applications requiring a detailed understanding of synoptic scale temperature fluctuations in this region.

3.4. Horizontal and vertical scales of thermal variations

Using all available SST data and surface air temperature station data south of 61.5 °N, we separately assessed the oceanographic and atmospheric decorrelation length scales for temperature anomalies at synoptic ($T^{'}_{HP}$) and seasonal-to-interannual time scales ($T^{'}_{LP}$), as well as the annual mean (T_{DC}) (Fig. 9). Methods identical to those used for the oceanographic data were used to calculate $T^{'}_{HP}$, $T^{'}_{LP}$ and T_{DC} for the atmospheric data. For $T^{'}_{HP}$, the atmosphere retains a higher level of covariability over length scales up to $\sim\!\!750$ km. Both the ocean and the atmosphere exhibit very strong covariability of T_{DC} . The correlation for $T^{'}_{LP}$ drops to $r \leq 0.5$ (25% of the variance) for station separations $> \sim\!\!1000$ km for both the ocean and the atmosphere.

The four ocean station pairs with a separation distance 1–10 km have a synoptic-scale correlation of $\sim\!0.75\!<\!r<0.85.$ Nearly all ocean stations separated by 10–30 km (50 unique station pairs) have a correlation coefficient of r<0.5 (eleven of the station pairs in this range show

0.5 < r < 0.8). These results show that the day-to-day variability of ocean station pairs separated by only a few tens of km can be extremely large.

The cross-correlation of air temperatures for T^{\prime}_{LP} and T^{\prime}_{HP} exhibit negative correlations for length scales greater than 2000 km, a separation distance that only occurs for stations near the outer edges of our domain. We interpret this behavior as being associated with the horizontal length scale of large atmospheric storm systems, which are associated with poleward winds on their eastern flank and equatorward winds on their western flank. Hence, cyclones that lie within the bounds of our station range exert a differential advective influence on station air temperatures. When a low-pressure system advects warm southern air masses into the eastern Gulf of Alaska, it also advects cooler high latitude air into the western Gulf of Alaska and along the Aleutian Islands. Interestingly, this character is observed for both the synoptic and seasonal frequency bands.

We next assess the correlation of monthly temperature anomalies for surface and subsurface variations at four coastal CTD profile stations: Kachemak Bay Transect 9 Station 6 (T09-06) in lower Cook Inlet, station GAK1 in the coastal waters of the outer Kenai Peninsula, station KIP2 in western PWS, and station GLBA-20 in Glacier Bay.

The results (Fig. 10) generally exhibit higher correlations in the winter months, except for the deep (150–550 m depth) waters of KIP2. The correlation patterns during winter are consistent with our expectation of deeper winter mixed layers, decreased seasonal stratification and deeper wind-induced mixing at this time of year. Summer

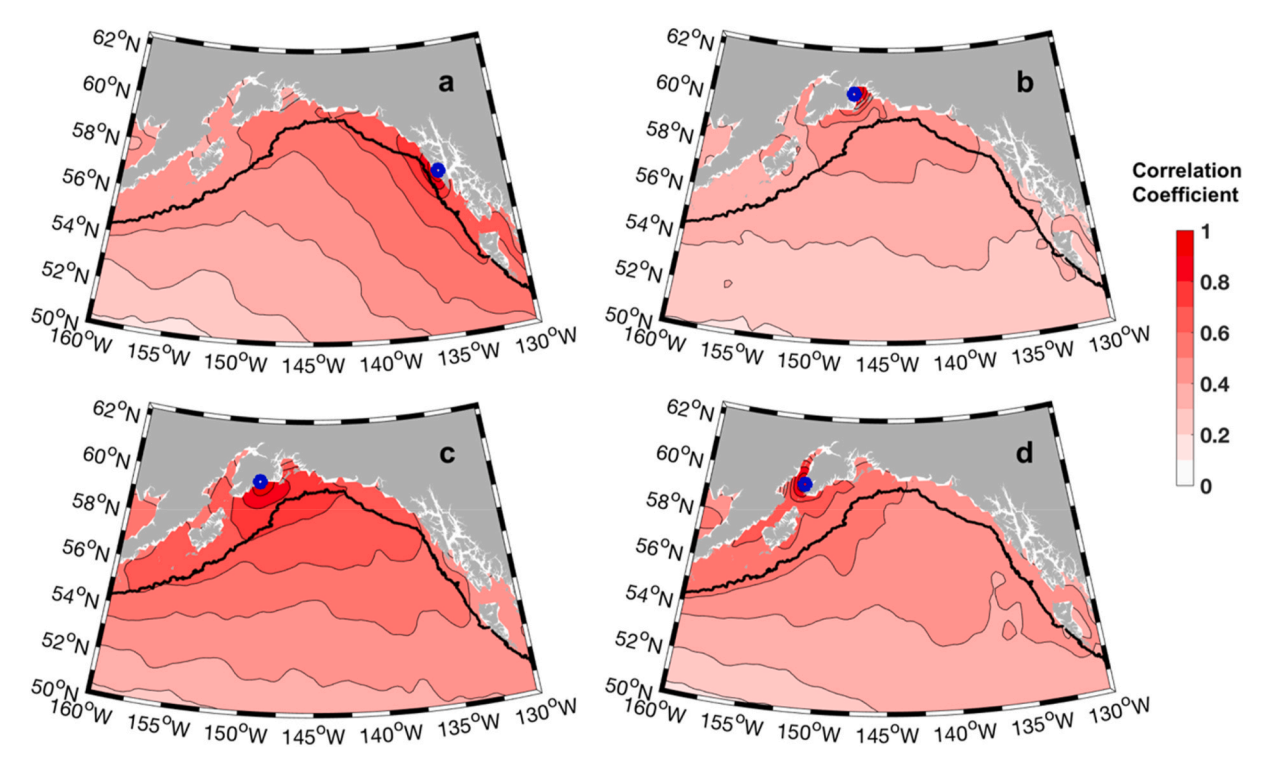


Fig. 7. Cross-correlation of the OISST temperature anomaly relative to reference points (blue circles) at Sitka (a), western Prince William Sound (b), GAK1 (c) and SWMP (d). The continental slope is denoted with a thick black contour at the 1000 m depth level.

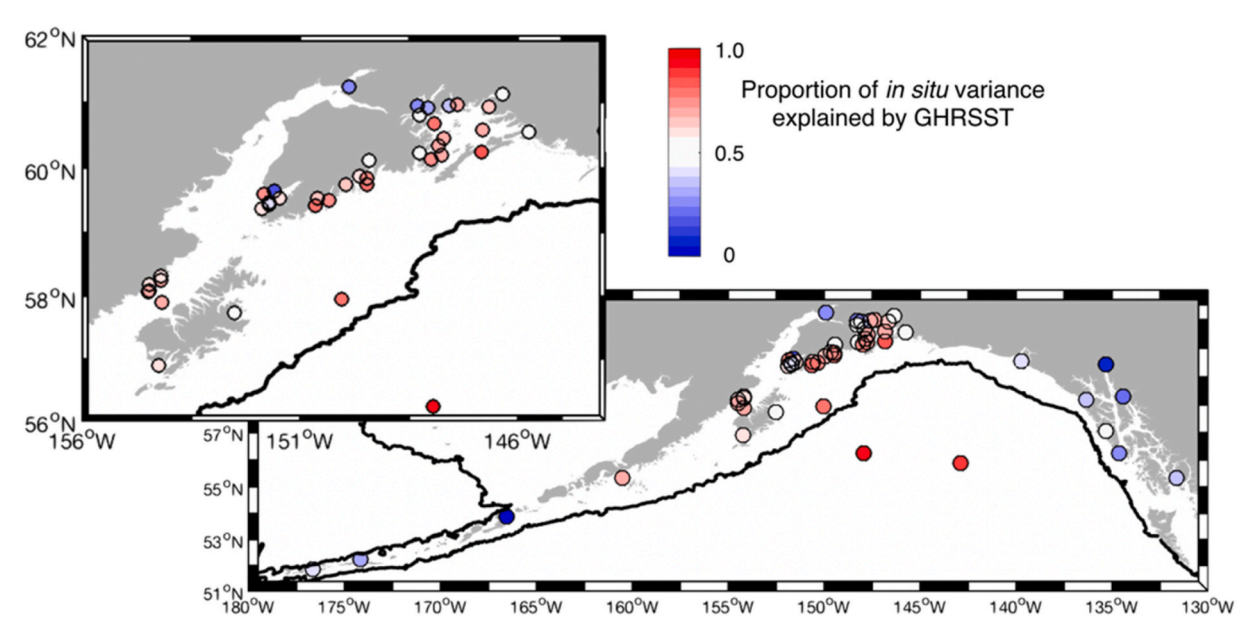


Fig. 8. Fraction of the in situ daily thermal anomaly variance explained by the GHRSST data. Thick contours locate the 1000 m isobath.

stratification decouples the upper and lower water column and thus degrades the surface-to-depth correlation at this time of year. Both KIP2 and GAK1 show correlation minima near 50 m depth and maxima near 150 m depth in summer, suggestive of systems with at least three functionally distinct layers. The upper layer warms in concert with surface heating, the middle of the water column may adjust relative to interior Ekman return flows and the lower layer warms due to the deep inflow associated with the summer relaxation of downwelling winds (Weingartner et al., 2005). The shallowest of the four sites, KBAY6, shows the strongest correlations through the entire water column in both seasons, a characteristic consistent with strong tidally-induced

mixing in Cook Inlet.

KIP2 and GLBA20 are located in sheltered estuaries under the influence of strongly stratified water columns. In both seasons, these stations show strong declines in correlation between the surface and 10 m depth. At GLBA20, this very shallow stratified layer is also associated with cool thermal anomalies that covary in phase with fresh salinity anomalies in summer and fall months (not shown). More typically, warm anomalies (which correspond to greater rates of snow and glacier ice melt) are associated with fresh anomalies at coastal stations such as GAK1. Our interpretation is that the close proximity of GLBA20 and KIP2 stations to glaciers allows the CTD data from these stations to

S.L. Danielson et al.

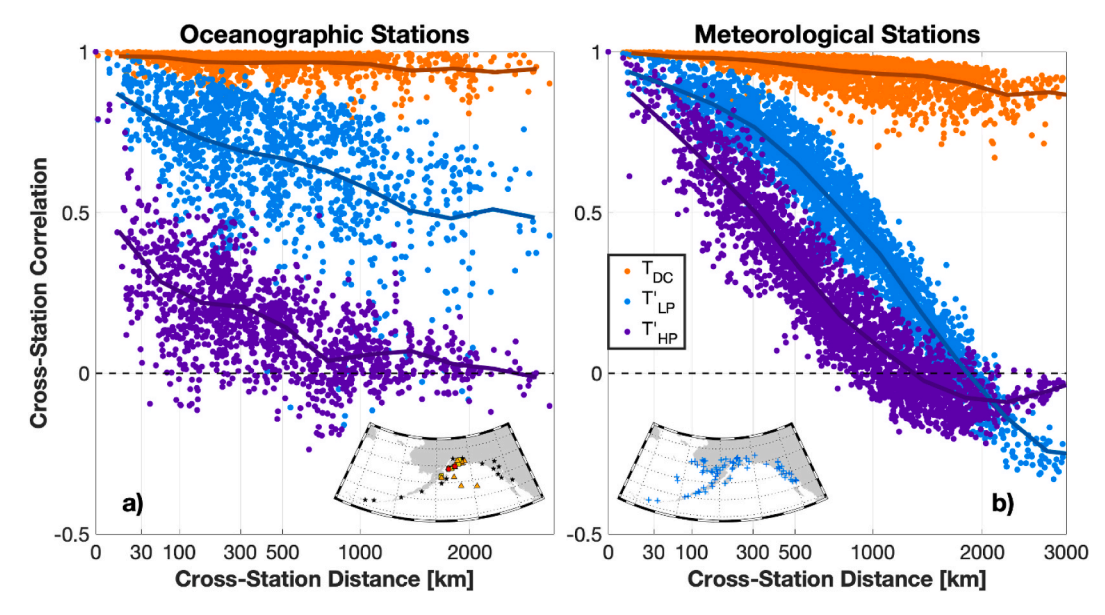


Fig. 9. a) Cross-correlation coefficient as a function of distance for all stations used in analysis (locations shown in inset map). Correlations between stations pairs are computed where the records have at least 1.5 overlapping years of data over the period from January 1, 2007 to May 1, 2018. Orange, blue and purple correspond to T_{DC} , T'_{LP} and T'_{HP} , respectively. Darker lines show bin averages. b) Same as (a), but for ASOS meteorological stations south of 61.5°N. See the Data and methods Section for abbreviation definitions.

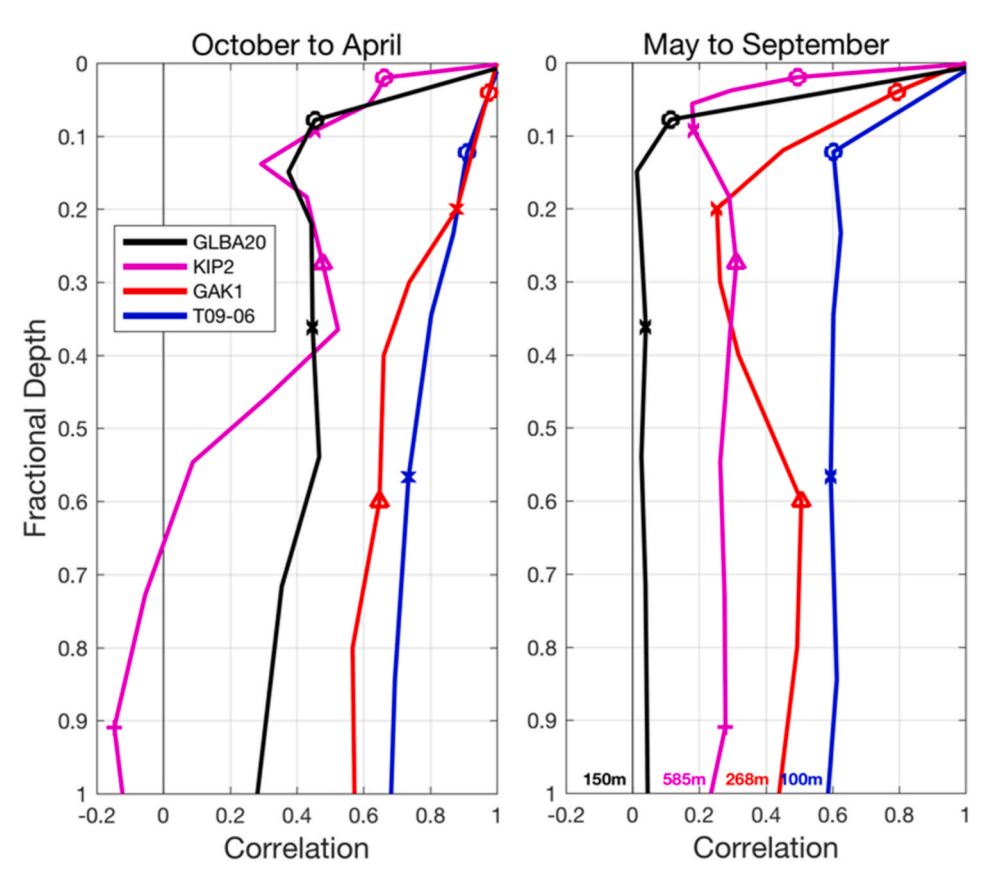


Fig. 10. Correlation between temperature anomalies at the surface and temperature anomalies at depths 0, 10, 20, 30, 50, 75, 100, 150, 200, 250, 300, 400, 500 and 550 m for cooling months (left) and warming months (right) as resolved by CTDs taken at stations GLBA20 (black), KIP2 (magenta), GAK1 (red) and the mid-transect station T09-06 in Kachemak Bay (blue). Symbols o, x, Δ , and + show the location of the 10, 50, 150 and 500 m depth levels, respectively. The seafloor depth of each station is noted at the bottom of the right-hand panel. Correlations are computed for the corresponding period of record for each site (50, 25, 22, and 7 years for GAK1, GLBA20, KIP2, and T09-06, respectively).

exhibit the influence of sensible heat directly associated with glacier meltwater, whereas more broadly a warm ocean and atmosphere induces excess snow and ice melt that increases runoff and freshening.

To show the nature of the covariability of surface and subsurface variations across the northern shelf, we examined the Seward Line CTD data from stations GAK1 through GAK13. We computed correlations

across all depths and all stations of the Seward Line relative to the surface temperature at GAK1 (Fig. 11a). We repeated the correlation analysis using the monthly climatology (10b) and monthly anomalies (10c). In all analyses, we found statistically significant inverse correlations between the surface at the coast and the outer shelf at depth, although the anomaly correlation noticeably weakens beyond the shelf

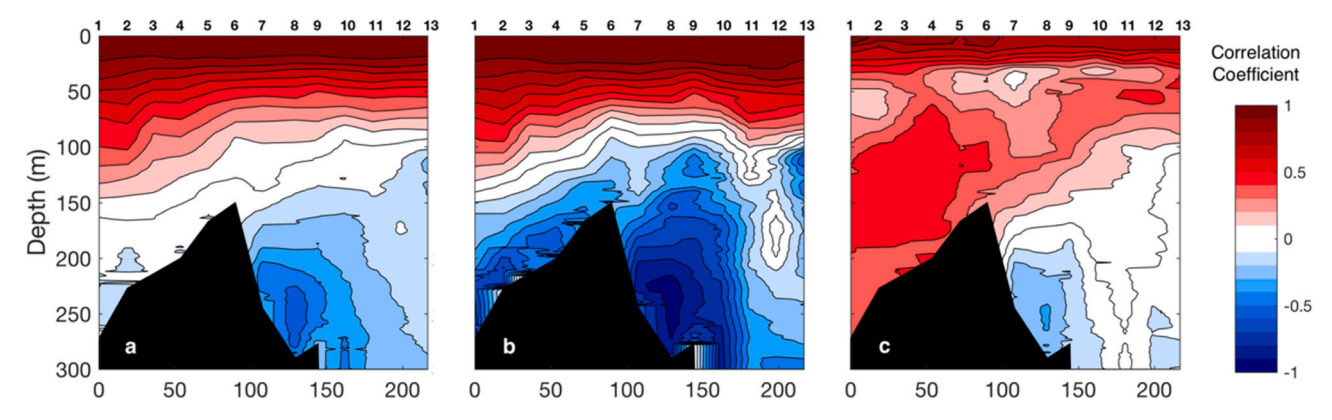


Fig. 11. Correlation of temperature across the Seward Line transect (station numbers locate GAK1 to GAK13 at the top of each panel) relative to the surface temperature at station GAK1. Panel (a) shows correlations that characterize the observed temperatures. Panel (b) depicts the correlation of the monthly climatology. Panel (c) shows correlations of the monthly anomalies (monthly climatology removed). Black regions depict the shelf seafloor. Correlations are computed here for 103 Seward Line occupations between 1974 and 2021.

break (station GAK9) where the Seward Line extends into the Alaska Current. The correlations show a strongly layered structure. An anomaly correlation minimum observed between about 50 and 75 m depth near GAK1 shoals farther offshore to approximately 30–40 m depth, following the offshore shoaling of isopycnals (not shown).

Fig. 11 spatial patterns relate to the structure and behavior of the shelf-break front, which typically intersects the outer shelf seafloor between 200 and 300 m depth (Okkonen et al., 2003; Weingartner et al., 2005). While the seasonal climatology shows out-of-phase relations between the surface and the seafloor (10b), temperature anomalies tend to vary in-phase inshore of station GAK7 and in the upper water column offshore of this station (10c).

At 250 m depth at the shelf break, we find that temperature and salinity are significantly and inversely correlated (r = -0.54, p < 0.001).

Given the known positive correlation between nutrients and salinity (Childers et al., 2005; Mordy et al., 2019), the panels of Fig. 11 suggest that the negative temperature anomalies depicted at the seafloor near the shelf break are also associated with positive nutrient concentration anomalies. The portion of the shelf located between stations GAK6 and GAK9 spans the eastern flank of Amatuli Trough (Fig. 2), indicating that near-bottom along-isobath flows at these stations are primarily directed toward the inner shelf and therefore represent an onshelf-flux of salt and nutrients.

3.5. Linking the nearshore and coastal realms

The results in Section 3.3, based on *in situ* station data, show that thermal covariation degrades with increasing distance both laterally and

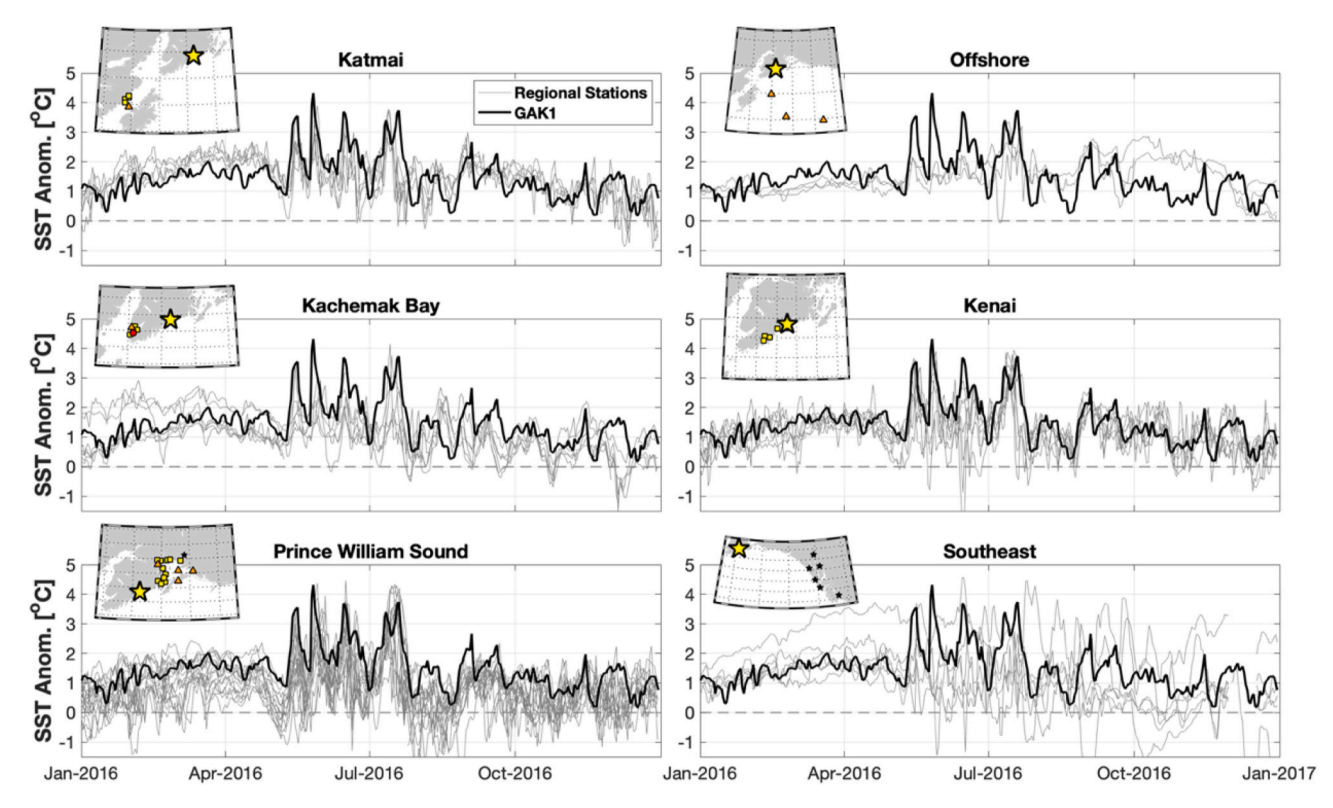


Fig. 12. Temperature records with the annual cycle removed (T_{RAW} - T_{DC}) at GAK1 (black line) and all other stations (grey lines) for six sub-regions during year 2016. The mean annual cycle is computed by using (sometimes incomplete) data records spanning January 1, 2007 to May 1, 2018. Inset maps show stations used for each region (in color, identical to Fig. 2). The yellow star locates GAK1.

with depth through the water column. However, five of our primary focal sub-regions (Katmai, offshore Gulf, Kachemak Bay, Kenai Peninsula, and PWS) exhibit a considerable degree of synoptic scale covariability (Fig. 12), and even the more distant and geographically isolated sixth sub-region, SE Alaska, also does to a lesser extent.

GAK1, centrally located relative to the intertidal and coastal stations, is well correlated with the daily SST anomaly across relatively large distances (Fig. 7) and provides a 5-decade record that is suitable as a baseline reference. Corrected for varying time series durations that unequally cover years, we find that GAK1 is warmer than most of the intertidal locations (Fig. 13). This characteristic likely reflects the closer connectivity of GAK1 to the shelf circulation, where waters are advected along-shore from warmer sites to the south, versus nearshore sites, which are shallower and subject to strong local heat losses. The coldest sites tend to be nearer to tidewater glacier influences and/or downstream of Cook Inlet outflows. In particular, the Harris Bay site in Kenai Fjords and the Whale Bay, Bettles, Esther and Unakwik sites in PWS have the closest proximity to tidewater glaciers in their respective regions. Relative to Cook Inlet, the Bluff Point and Bishop Beach sites (see Table S1 for precise site locations) are located near the western edge of Kachemak Bay and are most directly connected to the lower Cook Inlet throughflow while all the Katmai sites are located downstream of Cook Inlet. We also note that Janout et al. (2013) showed enhanced rates of surface heat losses in the western Gulf of Alaska from Cook Inlet to Unimak pass, relative to the northern and eastern portions of the shelf.

The analysis of variance for T_{DC} (annual cycle), T'_{LP} (temperature anomaly low-pass filtered at 30 days) and T'HP (temperature anomaly high-pass filtered at 30 days) at each site and referenced to GAK1 are shown by the Taylor diagram (Taylor, 2001) in Fig. 14. The annual cycle at all sites is well captured by TDC (orange symbols in all sections of Fig. 13, S4 and S5), with most stations showing r > 0.95 relative to GAK1, with the weakest correlations found in SE Alaska, along the Aleutian Islands, and in upper Cook Inlet (Anchorage). The scatter of T'_{LP} evenly about $\sigma = 1$ shows that the GAK1 variance magnitude is typical of the mean of the other stations. The RMSD of the data (concentric circles about GAK1) shows that the typical magnitude of

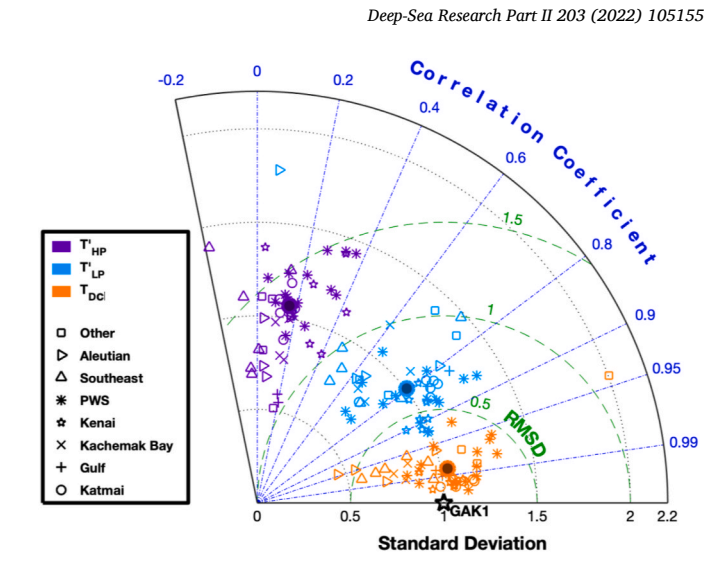


Fig. 14. A Taylor diagram (Taylor, 2001) representation of correlation analysis (azimuthal coordinate) between sea surface temperature anomalies at GAK1 and all other stations, normalized standard deviations (radial distance from origin) and their root mean square difference (RMSD, radial distance from the GAK1 reference point). Symbol shape denotes the region of each station (PWS = Prince William Sound); colors distinguish the three frequency bands. Standard deviations for all stations are normalized by the standard deviation at GAK1. RMSD and σ are both unitless. Analyses represent the period of station record overlap with that at GAK1. Dark circles show averages for each temporal band.

error for T_{DC} is small, often RMSD<0.4.

T'_{LP} (blue symbols in Fig. 14) is less well correlated than T_{DC}, typically 0.2<r < 0.6, but still the relations remain statistically significant (p < 0.05) for the most part. GAK1 shows little bias relative to the other stations. T'HP (purple symbols in Fig. 14) are only weakly correlated to those at GAK1, indicating that day-to-day temperature fluctuations do not covary amongst sites. In both $T^{\prime}_{\,LP}$ and $T^{\prime}_{\,HP},$ regional differences are evident in Fig. 14, S4 and S5, with the tendency for closely spaced

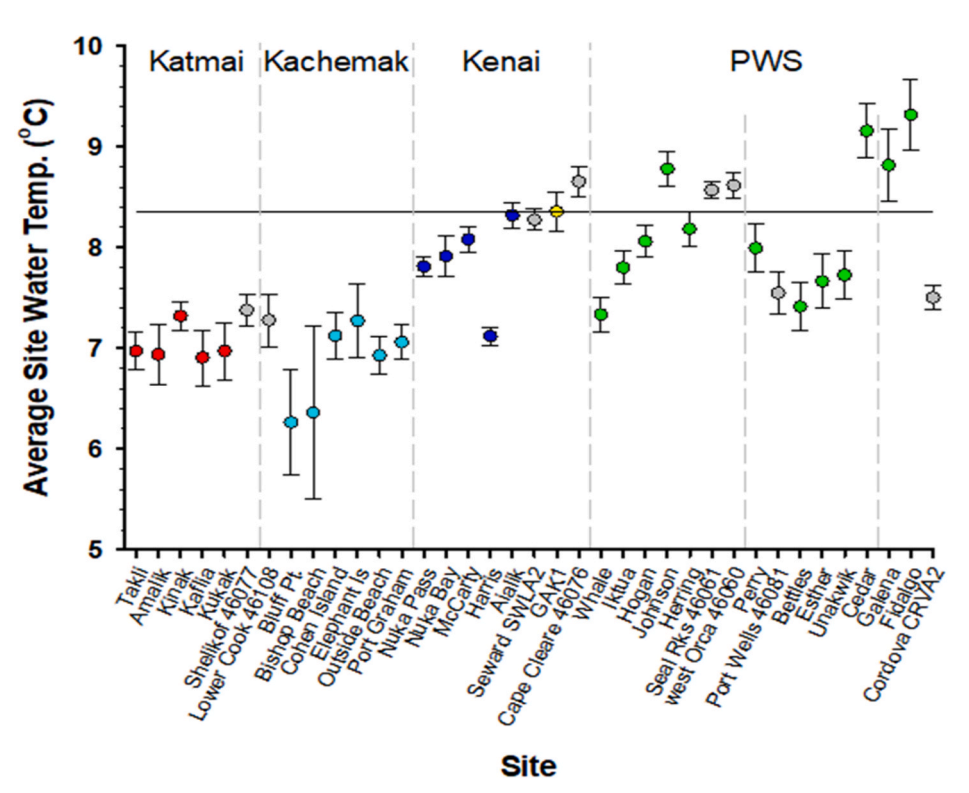


Fig. 13. Long-term mean temperature measured at the nearshore HOBO sites and select coastal stations along with 95% confidence intervals. Means are each baseline-adjusted to account for varying length time series and are shown relative to a 1970-2019 GAK1 reference (yellow circle, marked by the horizontal line). Red, cyan, blue and green symbols denote HOBO sites in Katmai, Kachemak Bay (Kachemak), Kenai Fjords (Kenai) and Prince William Sound (PWS), respectively. Grey symbols denote coastal NOAA buoys. PWS is further divided into western, northern, and eastern areas.

stations to exhibit similar behavior to each other.

To assess the covariability between sites within each of the focal subdomains, we selected regional reference stations (choosing the station best correlated with GAK1 from within each domain) and repeated the above analyses (Fig. S5). We found that stations within most of the domains each exhibit stronger covariation to the local reference than to the GAK1 reference. Most show $r \geq 0.99, \, r > 0.8$ and r > 0.3 for $T_{DC}, \, T^*_{LP}$ and T^*_{HP} , respectively. The SE Alaska domain and offshore regions are notably less well correlated with $r{\sim}0.98,\, 0.6$ and 0.1 for the three frequency bands, respectively, although stations here are more spatially dispersed and geographically isolated than within the other domains (see Fig. 2).

In addition to cross-station covariability, it is also informative to examine station temporal autocorrelation functions. The typical decorrelation time scale (τ_0), calculated using the first zero crossing of a record's autocorrelation function is about 9–13 days in winter and 8–11 days in summer. Longer time scales occur offshore and at coastal sites (Katmai, GAK1) where along-shore advection is important. The more protected sites (Kachemak Bay) tend to have shorter decorrelation time scales, suggesting stronger local influences on temperature. The decorrelation time scale results are also consistent with our expectation that nearshore realms exist within relatively large lateral gradients. The fact that most estimates of τ_0 fall within the timescale of the fortnightly spring-neap cycle suggests a role for tide-induced mixing in helping to set local conditions.

In summary, spatial variability of surface temperature fluctuations varies greatly at synoptic time scales in the nearshore realm, even between sites separated by as few as $\sim\!10$ km. In contrast, over seasonal and interannual time scales, temperature anomalies are well correlated for station separations of many hundreds of kilometers. Hence, monitoring of individual bays is important if it is critical to differentiate local, day-to-day temperature variations. On the other hand, few NGA monitoring stations are required to document seasonal and longer period anomalies, which tend to manifest in-phase and broadly across regional and basin scales (e.g. $100{-}1000$ km). The above insights of temporal and spatial structure in the temperature fluctuations provides a foundation for us to more closely examine warm and cool temperature anomalies through months, seasons and years (Fig. 15).

3.6. The pacific marine heatwave

The PMH was first observed in the central Gulf of Alaska, emerging as a highly unusual warming event confined to the upper 100 m of the water column in late fall 2013 but continued strengthening through winter 2014 (Freeland, 2014). By the end of 2015 the surface heat anomaly had penetrated across the upper 300 m of the central Gulf, where it persisted with positive heat content anomalies into 2018 (Jackson et al., 2018; Ross et al., 2019). In this section, we examine how the PMH and subsequent warm anomalies (e.g. Fig. 15) manifested on the NGA shelf and nearshore zone.

Nearly all intertidal and coastal SST time series across the various NGA regions depict a coherent pattern of seasonal to interannual variability (Figs. 11 and 14), with prominent peaks and troughs roughly coincident at these time scales. Figs. 5 and 14 depict two distinct temperature regimes for the 2006 to 2019 time period: a cool interval from 2006 to 2013 and a warm interval from 2014 to 2019. Nearly all sites experienced warming through calendar year 2013. At station GAK1, a multi-year cool interval persisted below 100 m depth throughout 2013 although surface anomalies turned positive. However, by early 2015 the entire water column (250 m) showed large positive anomalies at GAK1. This was followed by a cooling interval through late summer 2015 although temperatures still remained above normal. A strong El Niño event contributed to even warmer conditions in 2016 (Gentemann et al., 2017). Below, we examine additional aspects of the temporal synchrony of the preceding cool phase, the warming transition that led to positive thermal anomalies, and the surface heat fluxes that drove these

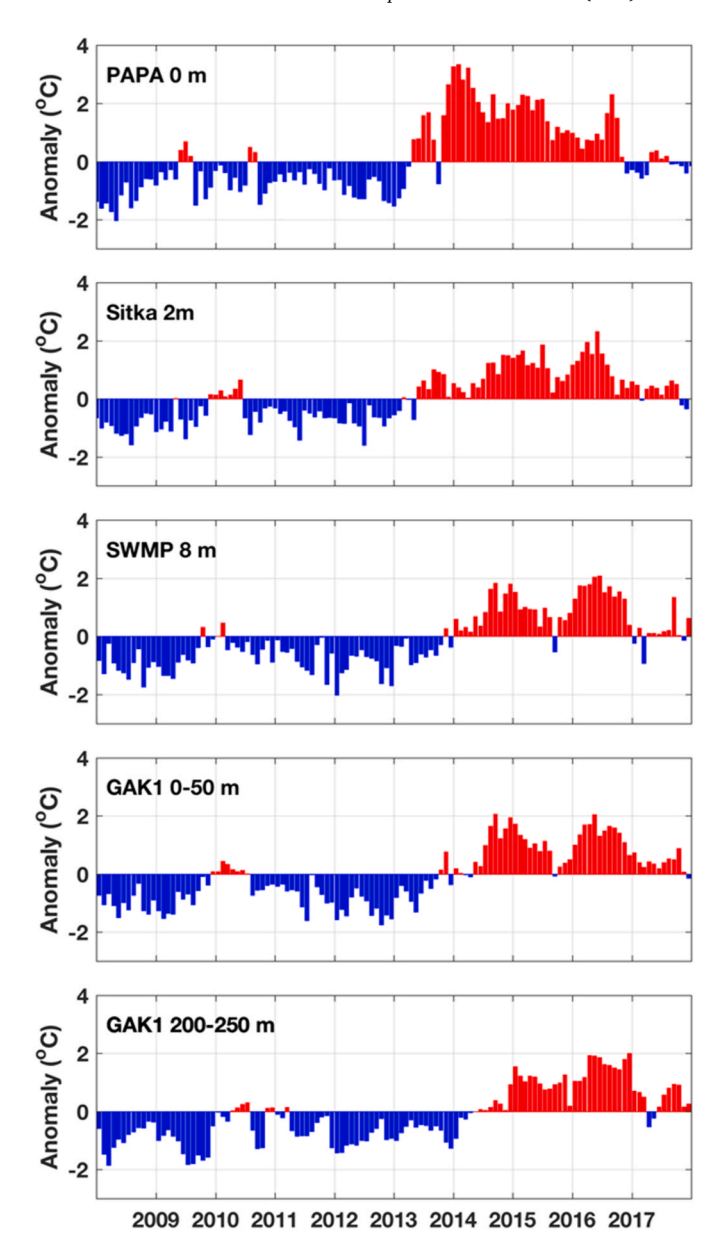


Fig. 15. Monthly temperature anomalies at ocean station PAPA (from the OISST record), the Sitka tide gauge station, SWMP mooring and GAK1 over 2008–2017. Anomalies are all referenced to the same 2008–2019 baseline.

anomalies.

Eleven SST timeseries in our data compilation are from stations that also have a nearly co-located ASOS weather station. These are nearly evenly distributed around rim of the Gulf of Alaska from Adak Island in the Aleutians to Port Alexander in SE Alaska. Observed quantities at these stations include air temperature, relative humidity, wind speed and cloud cover. Coupled with the measurements of SST, these records provide sufficient information to compute local bulk surface heat flux terms.

Due to a dearth of hydrographic profile and velocity data that are both seasonal and proximate to the eleven selected stations, it is not possible to reasonably constrain direct estimates of mixed layer depths nor advective and diffusive terms. Nevertheless, estimating the net surface heat flux (Q_{SUM}) remains informative as it allows us to assess the importance of local surface forcing relative to observed changes in near-surface ocean temperature. To provide a rough sense of the rate of change in upper ocean heat content (Q_{OC}) , we assumed that changes in near-surface temperature were uniform over the upper 15 m, a

commonly observed NGA summer month mixed layer depth.

We find that the annual cycle of Q_{OC} and Q_{SUM} are reasonably similar in both magnitude and phase (Fig. 16). Frequently Q_{SUM} has a negative offset relative to Q_{OC} , potentially implying a supply of heat from diffusive or advective processes.

The monthly anomalies of Q_{OC} and Q_{SUM} are significantly correlated (p < 0.05) for six of the eleven stations used for heat flux analysis, though none have correlation coefficients greater than 0.5. This suggests that the terms in Q_{SUM} have only a modest degree of influence on NGA heat content and that other drivers dominate. Stations close to the ACC may be heavily influenced by the advective terms, and diffusive terms may be of first order importance at stations near regions of particularly strong tidal mixing (e.g. Portlock Bank, the Aleutian Islands). The assumption that temperature changes are uniform over the upper 15 m is clearly an oversimplification, since mixed layer depths vary seasonal and spatially, and thus are a factor contributing to the low correlations between the anomalies of Q_{OC} and Q_{SUM} .

To assess the temporal patterns of surface heat fluxes (Q_{SUM}) across the whole NGA, we used the estimates at the eleven stations to compute the total annual heat flux anomaly (annual cycle removed) for each year (Fig. 17). Anomalous heating occurred in 2009, 2013 and 2014, while 2008, 2011 and 2017 have significant cooling anomalies. These results are in close agreement with the year-to-year changes of heat content suggested by Figs. 4 and 15. The surface forcings that triggered the 2006–2013 cool phase were associated with anomalies in coastal runoff, winter cooling, stratification and winds associated with an eastward-shifted Aleutian Low relative to warmer years (Janout et al., 2010).

We can assess the importance of the estimated 2013 heat flux anomaly (Fig. 16; \sim 11 W m⁻²) relative to the observed magnitude of warming. The change in water column temperature (ΔT) over one year

(Δt) can be estimated as $\Delta T = (Q_{SUM}\Delta t)/(\rho C_P H)$ where $C_P \sim 4000 \ J^{\circ} C^{-1} \ kg^{-1}$ is the heat capacity of seawater, $\rho = 1025 \ kg \ m^{-3}$, and $H = 15 \ m$. We find $\Delta T = 5.6 \ ^{\circ} C$, which is much larger than the temperature increase seen at any nearshore or coastal station in 2013, so we can deduce that the heat must have been mixed much deeper than the upper 15 m or advected out of the system. For a typical shelf depth of 200 m in the NGA, the warming implied by this heating rate was 0.42 $^{\circ} C$. This value is appreciably smaller than observed temperature changes during our period of interest (Fig. 15).

Assuming the additional warming is due to advection of warm southerly or offshore waters, we can make a crude estimate of the current speed needed to supply the remaining heat. Starting with the simplified framework that heating occurred uniformly over the \sim 150 km wide and \sim 200 m deep shelf (e.g. Fig. 15), the current speed (u) can be deduced from the simple advective equation, $\Delta T = u(dT/dx)\Delta t$. We assume that the warming (ΔT) of 1.5 °C occurs over 1 year (Δt) and the lateral temperature gradient is on the order of 1 °C per 1000 km. The derived current speed is \sim 5 cm/s. Though the approximations used in this construction make it an order of magnitude estimate only, the scale is reasonable relative to the dimensions of the Gulf of Alaska and relative to the magnitude of expected subtidal currents (e.g. Stabeno et al., 2016).

The heat fluxes estimated from the *in situ* SST/ASOS stations are also roughly congruent in timing, magnitude and sign with NCEP-R2 estimates of heat flux in the NGA (Fig. 18). Except for 2009 (a year of anomalously strong downward shortwave radiation), between 2006 and 2012 the NGA experienced weak to moderate cooling before the strong warming in 2013 triggered the onset of the PMH that emerged in 2014. Early in this cool phase, the temperature decline was associated with strong ocean-to-atmosphere heat loss in November 2006 and March

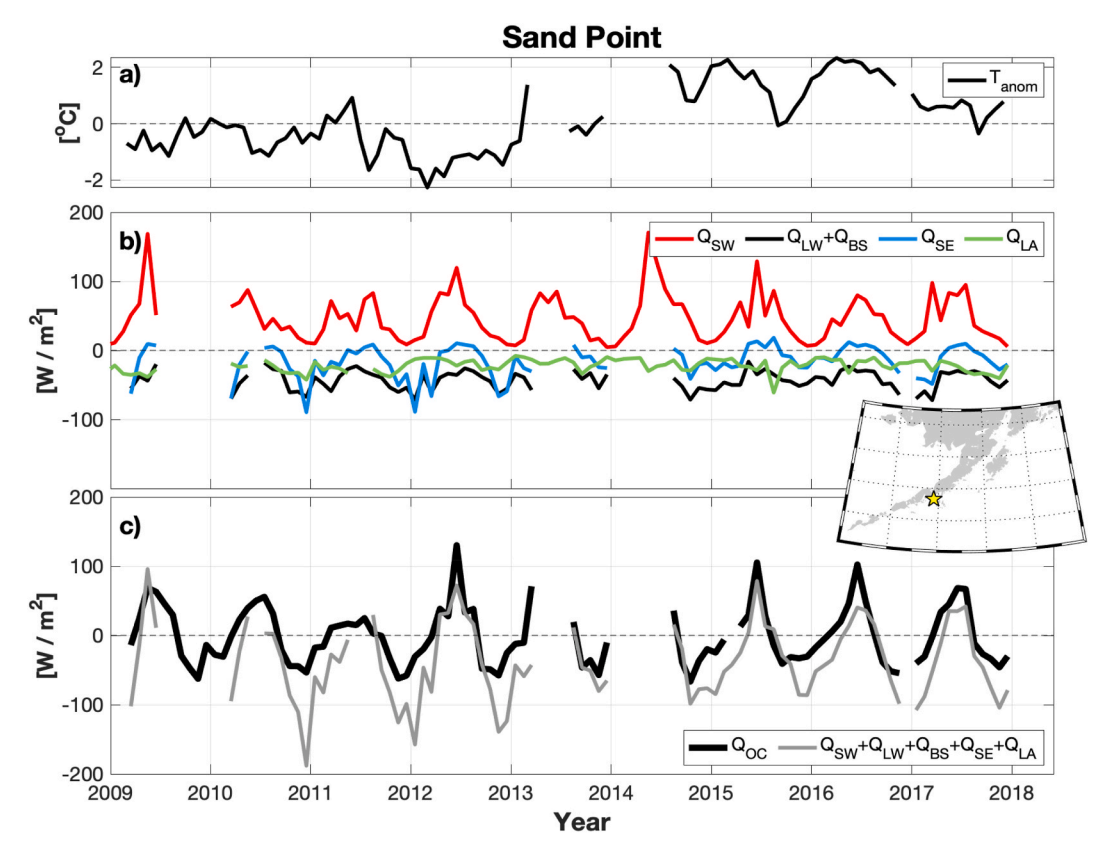


Fig. 16. a) Monthly sea surface temperature (SST) anomaly (monthly average removed) for the Sandpoint tide gauge station. Anomalies were calculated between January 1, 2007 and January 1, 2018. b) Heat flux terms (W m $^{-2}$) computed from the tide gauge station, an ASOS weather station, and NCEP-R2. Downward shortwave radiation (Q_{SW}) is computed from 6-h averages of clear-sky NCEP-R2. The combined longwave (Q_{LW}) and backscatter (Q_{BS}) flux term is derived from both tide gauge SST and weather station data, as are the sensible (Q_{SE}) and latent (Q_{LA}) terms. c) Heat flux of the ocean (Q_{OC}) assuming the changes in SST are uniform over the upper 15 m and the sum (Q_{SUM}) of the terms in panel (b). The inset map shows the location of the Sand Point station (yellow star).

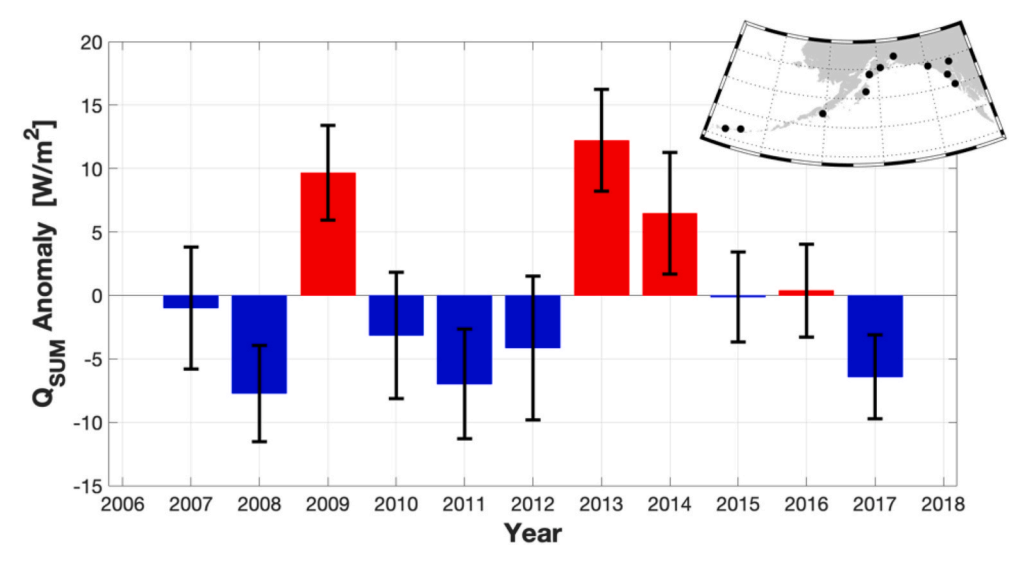


Fig. 17. Annual averages of the anomaly of Q_{SUM} (annual cycle from 2007 to 2017 removed) for all sites with oceanographic and Automated Surface Observing System weather stations in close proximity (inset map). Error bars show the 95% confidence interval.

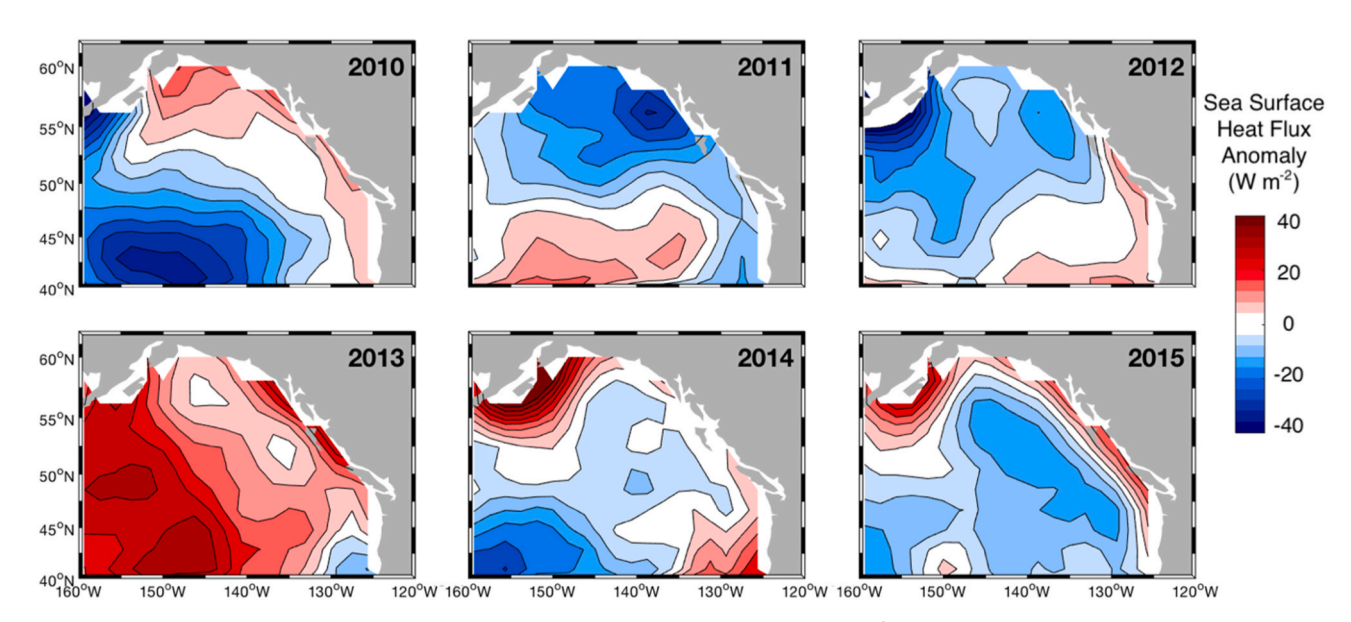


Fig. 18. NCEP-R2 estimates of the annual mean net surface heat flux anomaly (W m⁻²) for 2010 to 2015 over the NE Pacific.

2007 and below-average runoff in fall (Janout et al., 2010). Together, winter surface heat fluxes and salinity stratification can explain over 80% of thermal variations below 100 m depth at station GAK1 (Janout et al., 2010). The NCEP-R2 distribution of surface heat fluxes suggest that anomalous warming was mostly confined to the northern shelf in 2014 and 2015, albeit with a larger magnitude in 2014. This signal stands in contrast to the near zero or negative heat flux anomalies found offshore in these two years. Hence, while the central Gulf of Alaska upper water column was being forced back towards mean conditions in 2014 and 2015 by atmospheric heat fluxes (but remaining warmer than usual), the shelf regions did not experience anomalously negative atmospheric heat fluxes until 2017 (Fig. 17).

While all of the stations shown in Fig. 15 warmed in 2013 at the surface (GAK1 did not warm at depth), the surface temperature at Ocean Station PAPA near the geographical center of the "blob" (Bond et al., 2015) increased much more rapidly than the Alaskan coastal stations. Furthermore, while the warming signal at PAPA peaked in early 2014, warming over the shelf continued until mid-late 2014, peaking in late summer at the surface, and in January 2015 near the seafloor at GAK1.

Temperatures near the seafloor at GAK1 commonly lag temperature signals observed in the upper water column (Royer, 2005; Weingartner et al., 2005) and this was true for the PMH signal (Fig. 15). Near-bottom temperatures abruptly warmed in January 2015 and remained elevated by nearly 1 $^{\circ}$ C above normal until early spring 2016 when they further increased to near 2 $^{\circ}$ C above normal (Fig. 15). Warming associated with the 2015 El Niño contributed to increased temperatures in the NGA in 2016, and GAK1 remained above normal throughout 2017, 2018 and 2019 (Fig. 4).

4. Conclusions and summary

This combined analysis of anchored, buoy, moored, ship-based, remotely sensed, and reanalysis data provides new insights to the nature of spatial and temporal thermal variations in the NGA.

Long-term air temperature records from Sitka, the ERSST blended product and GAK1 water column profile data provide a climatic context for our study. We find long-term warming trends in the NGA SST and Sitka air temperature datasets that are statistically indistinguishable (see

Section 3.1), a result that conforms with the strongly marine-dominated climate found at Sitka. All three of these temperature records provide some predictive power for following-year marine water temperature anomalies at GAK1, suggesting potential application to forward-looking fish stock recruitment models. The leading-year relationship of the Sitka air temperature, which is the best predictor of the three, may reflect in part its upstream location relative to the GAK1 site.

Our analyses show that NGA nearshore, coastal and offshore SST anomalies tend to exhibit synchrony at seasonal and longer time scales, with station-to-station correlations generally greater than 0.5 for separations up to $\sim\!1000$ km, whereas synoptic scale nearshore variability is poorly correlated after only 10–30 km (Fig. 9). While satellites are valuable for capturing seasonal and longer temperature variations, their accuracy in the nearshore and coastal realms degrades significantly on daily temporal scales (especially during north-to-south flight trajectories), with up to 30–40% of the variance (random errors of $\pm0.5~^{\circ}\text{C}$) unresolved when compared to in situ observations (Fig. 8).

Our results suggest potential tradeoffs between the effort of monitoring, the methodological approach, and the benefits of the available data. While not all reference sites are as representative of the greater shelf as others, all stations do generally capture the large-scale seasonal and sub-seasonal signals that dominate interannual variability (Fig. 14). Hence, only a few broadly distributed monitoring stations are required to capture regional thermal variability. However, quantifying thermal variations at time intervals of less than 1 month at even relatively closely spaced stations requires closely spaced dataloggers.

Biological productivity is often high in many nearshore and coastal regions, so ecosystem studies that seek to mechanistically link environmental conditions to abundance, biomass and community composition may not be able to rely solely on satellite measures of temperature, and in these locations the relative importance of *in situ* measurements increases. Similarly, the co-variability of temperature fluctuations degrades rapidly with depth (Fig. 10). Thus, measures of SST alone may be insufficient to fully characterize even nearshore habitats.

Beyond diminished correlation at depth, analysis of CTD profiles shows that near-bottom temperature anomalies over the outer shelf exhibit a negative correlation with surface thermal anomalies and near-bottom salinity anomalies (Fig. 11). As salinity and nitrate exhibit a positive relation in the NGA (Childers et al., 2005), the inverse correlation of thermal and haline anomalies suggests that positive surface temperature anomalies are associated with elevated nutrient anomalies at depth. These signals were observed at the upwelling-favorable side of Amatuli Trough where flows near the seafloor will generally be directed onto the shelf. This linkage deserves closer investigation because if the relation is due to coupling by the ocean current field, it could provide a means for the long record of surface temperature data to serve as a proxy for cross-shelf nutrient flux anomalies.

The patterns of thermal variability examined here can offer insights into the role that thermal conditions play in driving biological communities. For example, in the intertidal zone, species such as the Pacific blue mussel (Mytilus trossulus), are abundant consumers with growth characteristics tightly coupled to their habitat temperature. Before the onset of the recent PMH, intertidal invertebrate and algal community structure and dynamics appeared to vary independently among observations in our focal regions (PWS, Kenai Fjords, Kachemak Bay and Katmai), suggesting that intertidal community structure is largely driven by local dynamic drivers (Konar et al., 2016). Temperatures did not become anomalously high in the nearshore zone until mid to late summer 2014 (Fig. 15) and, correspondingly, the intertidal community structure showed no change in early summer of 2014 (Weitzman et al., 2021). However, by the summer of 2015, intertidal macroalgae biomass (primarily Fucus distchus) declined, which increased the amount of open space available for settlement of intertidal organisms. This, in turn, led to a successional sequence that moved community composition towards a more similar structure across all regions through time (Weitzman et al., 2021). For example, barnacle cover increased in 2016, followed by

an increase in mussel cover by 2017, and finally, a slow return of *Fucus* by 2018 and 2019 as temperatures declined from the heights of 2015 and 2016 (Weitzman et al., 2021). This sequence of events represented a shift in the intertidal communities across the Gulf of Alaska from one dominated by macroalgae to one dominated by filter-feeding invertebrates. These changes in community structure aligned with the timing of the PMH effects, suggesting that large-scale oceanographic and atmospheric forcing can override local drivers to regionally influence patterns of intertidal community structure (Weitzman et al., 2021).

While temperature is a key variable that helps regulate biological activity, other factors that we have not considered in great detail also play defining roles in setting habitat character and quality. Clearly, a comprehensive understanding of thermal variations is incomplete without consideration of the advective-diffusive environment, stratification, and especially salinity. Because stratification and associated advective features are controlled by salinity rather than temperature in subarctic seas such as the NGA, disentangling the influence of thermal variability on the physical system and the ecosystem can only be done with additional consideration of the haline environment. For example, warming trends and associated longer, rainier winters will also advance the onset of springtime stratification over the inner shelf (Weingartner et al., 2005). Such local physical processes in the NGA can also have far reaching effects, as the ACC is an important freshwater source for the Bering Sea shelf and Arctic Ocean (Aagaard et al., 2006). Similarly, the influence of ocean flows around the biologically productive banks near Kodiak Island and along the continental slope are also likely important contributors to the character of the local thermal field. This analysis provides a foundation upon which these other necessary studies can be conducted in the future.

Declaration of competing interest

The authors declare that they have no known competing financial interests or personal relationships that could have appeared to influence the work reported in this paper.

Acknowledgements

The authors thank the many students, researchers, and volunteers for assisting with intertidal surveys over the years; the Kachemak Bay National Estuarine Research Reserve staff who have assisted with our System Wide Monitoring Program; University of Alaska Seward Marine Center Staff David Leech and Peter Shipton for carrying out the GAK1 field program since 1999; the National Park Service for measurements from Glacier Bay; and the scientific team of the Gulf Watch Alaska longterm monitoring program for their expertise and resources in support of this publication. System Wide Monitoring Program data collection is supported financially by National Estuarine Research Reserve System operations with funding from NOAA to the Alaska Center for Conservation Science at the University of Alaska Anchorage, with technical and data management support provided by the National Estuarine Research Reserve System Central Data Management Office. We thank one anonymous referee and Tom Royer for review comments that improved the manuscript, and Royer for contributing the long-term Sitka air temperature time series. We also thank the full scientific team of the Gulf Watch Alaska long-term monitoring program for their expertise and resources in support of this publication. The research described in this paper was in part, supported by the Exxon Valdez Oil Spill Trustee Council under grant 21120114. Findings and conclusions presented by the authors are their own and do not necessarily reflect the views or position of the Trustee Council. The scientific results and conclusions, as well as any views or opinions expressed herein, are those of the authors and do not necessarily reflect those of NOAA or the Department of Commerce. Any use of trade, firm, or product names is for descriptive purposes only and does not imply endorsement by the U.S. Government. This manuscript has been approved for publication consistent with U. S. Geological

Survey Fundamental Science Practices (http://pubs.usgs.gov/circ /1367/). This research was also supported by the Alaska Ocean Observing System, the North Pacific Research Board (L37) and the National Science Foundation (OCE-1656070).

Appendix A. Supplementary data

Supplementary data to this article can be found online at https://doi.org/10.1016/j.dsr2.2022.105155.

References

- Aagaard, K., Weingartner, T.J., Danielson, S.L., Woodgate, R.A., Johnson, G.C., Whitledge, T.E., 2006. Some controls on flow and salinity in Bering Strait. Geophys. Res. Lett. 33 (19).
- Alexander, M.A., Deser, C., Timlin, M.S., 1999. The reemergence of SST anomalies in the north pacific ocean. J. Clim. 12 (8), 2419–2433.
- Anderson, P.J., Piatt, J.F., 1999. Community reorganization in the Gulf of Alaska following ocean climate regime shift. Mar. Ecol. Prog. 189, 117–123.
- Beamer, J.P., Hill, D.F., Arendt, A., Liston, G.E., 2016. High-resolution modeling of coastal freshwater discharge and glacier mass balance in the Gulf of Alaska watershed. Water Resour. Res. 52, 3888–3909.
- Bond, N.A., Cronin, M.F., Freeland, H., Mantua, N., 2015. Causes and impacts of the 2014 warm anomaly in the NE Pacific. Geophys. Res. Lett. 42 (9), 3414–3420.
- Cane, M.A., Zebiak, S.E., 1985. A theory for El Niño and the southern oscillation. Science 228 (4703), 1085–1087.
- Carmack, E., et al., 2015. The contiguous panarctic Riverine Coastal Domain: A unifying concept. Prog. Oceanogr. 139, 13–23.
- Chiang, J.C., Vimont, D.J., 2004. Analogous Pacific and Atlantic meridional modes of tropical atmosphere–ocean variability. J. Clim. 17 (21), 4143–4158.
- Childers, A.R., Whitledge, T.E., Stockwell, D.A., 2005. Seasonal and interannual variability in the distribution of nutrients and chlorophyll a across the Gulf of Alaska shelf: 1998–2000. Deep Sea Res. II 52 (1–2), 193–216.
- Chin, T.M., Vazquez-Cuervo, J., Armstrong, E.M., 2017. A multi-scale high-resolution analysis of global sea surface temperature. Remote Sens. Environ. 200, 154–169.
- Di Lorenzo, E., Mantua, N., 2016. Multi-year persistence of the 2014/15 North Pacific marine heatwave. Nat. Clim. Change 6 (11), 1042-1047.
- Di Lorenzo, E., Schneider, N., Cobb, K.M., Franks, P.J.S., Chhak, K., Miller, A.J., McWilliams, J.C., Bograd, S.J., Arango, H., Curchitser, E., Powell, T.M., 2008. North Pacific Gyre Oscillation links ocean climate and ecosystem change. Geophys. Res. Lett. 35 (8).
- Ding, R., Li, J., Tseng, Y.H., Sun, C., Guo, Y., 2015. The Victoria mode in the North Pacific linking extratropical sea level pressure variations to ENSO. J. Geophys. Res. Atmos. 120 (1), 27–45.
- Fewings, M., Lentz, S.J., Fredericks, J., 2008. Observations of cross-shelf flow driven by cross-shelf winds on the inner continental shelf. J. Phys. Oceanogr. 38 (11), 2358–2378.
- Freeland, H., 2014. Something odd in the Gulf of Alaska, february 2014. CMOS Bull. SCMO 42.
- Gabriele, C.M., Amundson, C.L., Neilson, J.L., Straley, J.M., Baker, C.S., Danielson, S.L., 2022. Sharp decline in humpback whale (Megaptera novaeangliae) survival and reproductive success in southeastern Alaska during and after the 2014–2016 Northeast Pacific marine heatwave. Mamm. Biol. 1–19.
- Gentemann, C.L., Fewings, M.R., García-Reyes, M., 2017. Satellite sea surface temperatures along the West Coast of the United States during the 2014–2016 northeast Pacific marine heat wave. Geophys. Res. Lett. 44 (1), 312–319.
- Harrell, F.E., 2001. Regression Modeling Strategies: with Applications to Linear Models, Logistic Regression, and Survival Analysis. Springer, New York, p. 608.
- Hare, S.R., Mantua, N.J., 2000. Empirical evidence for North Pacific regime shifts in 1977 and 1989. Prog. Oceanogr. 47 (2–4), 103–145.
- Hill, D.F., Bruhis, N., Calos, S.E., Arendt, A., Beamer, J., 2015. Spatial and temporal variability of freshwater discharge into the Gulf of Alaska. J. Geophys. Res. Ocn. 120 (2), 634–646.
- Hobday, A.J., Oliver, E.C., Gupta, A.S., Benthuysen, J.A., Burrows, M.T., Donat, M.G.,
 Holbrook, N.J., Moore, P.J., Thomsen, M.S., Wernberg, T., Smale, D.A., 2018.
 Categorizing and naming marine heatwaves. Oceanography 31 (2), 162–173.
- Hollowed, A.B., Hare, S.R., Wooster, W.S., 2001. Pacific Basin climate variability and patterns of Northeast Pacific marine fish production. Prog. Oceanogr. 49 (1–4), 257–282.
- Huang, B., Thorne, P.W., Banzon, V.F., Boyer, T., Chepurin, G., Lawrimore, J.H., Menne, M.J., Smith, T.M., Vose, R.S., Zhang, H.M., 2017. Extended reconstructed sea surface temperature, version 5 (ERSSTv5): upgrades, validations, and intercomparisons. J. Clim. 30 (20), 8179–8205.
- Jackson, J.M., Johnson, G.C., Dosser, H.V., Ross, T., 2018. Warming from recent marine heatwave lingers in deep British Columbia fjord. Geophys. Res. Lett. 45 (18), 9757–9764.
- Janout, M.A., Weingartner, T.J., Okkonen, S.R., Whitledge, T.E., Musgrave, D.L., 2009. Some characteristics of Yakutat Eddies propagating along the continental slope of the northern Gulf of Alaska. Deep Sea Res. II 56 (24), 2444–2459.
- Janout, M.A., Weingartner, T.J., Royer, T.C., Danielson, S.L., 2010. On the nature of winter cooling and the recent temperature shift on the northern Gulf of Alaska shelf. J. Geophys. Res. Ocn 115 (C5).

- Janout, M.A., Weingartner, T.J., Stabeno, P.J., 2013. Air-sea and oceanic heat flux contributions to the heat budget of the northern Gulf of Alaska shelf. J. Geophys. Res. Ocn 118 (4), 1807–1820.
- Joh, Y., Di Lorenzo, E., 2017. Increasing coupling between NPGO and PDO leads to prolonged marine heatwaves in the Northeast Pacific. Geophys. Res. Lett. 44 (22), 11–663.
- Kara, A.B., Hurlburt, H.E., Rochford, P.A., O'Brien, J.J., 2004. The impact of water turbidity on interannual sea surface temperature simulations in a layered global ocean model. J. Phys. Oceanogr. 34 (2), 345–359.
- Konar, B., Iken, K., Coletti, H., Monson, D., Weitzman, B., 2016. Influence of static habitat attributes on local and regional rocky intertidal community structure. Estuar. Coast 39 (6), 1735–1745.
- Ladd, C., Bond, N.A., 2002. Evaluation of the NCEP/NCAR reanalysis in the NE pacific and the Bering Sea. J. Geophys. Res. Ocn 107 (C10), 22-1.
- Ladd, C., Cheng, W., Salo, S., 2016. Gap winds and their effects on regional oceanography Part II: Kodiak Island, Alaska. Deep Sea Res. II 132, 54-67.
- Ladd, C., Kachel, N.B., Mordy, C.W., Stabeno, P.J., 2005. Observations from a yakutat eddy in the northern Gulf of Alaska. J. Geophys. Res. Ocn 110 (C3).
- Litzow, M.A., et al., 2020. Evaluating ecosystem change as Gulf of Alaska temperature exceeds the limits of preindustrial variability. Prog. In Oceanogr. 186, 102393.
- Litzow, M.A., Mueter, F.J., 2014. Assessing the ecological importance of climate regime shifts: an approach from the North Pacific Ocean. Prog. Oceanogr. 120, 110–119.
- Macklin, S.A., Bond, N.A., Walker, J.P., 1990. Structure of a low-level jet over lower Cook Inlet, Alaska. Mon. Weather Rev. 118 (12), 2568–2578.
- Mantua, N.J., Hare, S.R., Zhang, Y., Wallace, J.M., Francis, R.C., 1997. A Pacific interdecadal climate oscillation with impacts on salmon production. B. Am. Met. Soc. 78 (6), 1069–1080.
- Muench, R.D., Mofjeld, H.O., Charnell, R.L., 1978. Oceanographic conditions in lower Cook Inlet: spring and summer 1973. J. Geophys. Res. Ocn 83 (C10), 5090–5098.
- Mundy, P.R., 2005. The Gulf of Alaska: biology and oceanography. Univ. Alaska Sea Grant. 5 (No. 1).
- Mordy, C.W., Stabeno, P.J., Kachel, N.B., Kachel, D., Ladd, C., Zimmermann, M., Hermann, A.J., Coyle, K.O., Doyle, M.J., 2019. Patterns of flow in the canyons of the northern Gulf of Alaska. Deep Sea Res. II 165, 203–220.
- Okkonen, S.R., Weingartner, T.J., Danielson, S.L., Musgrave, D.L., Schmidt, G.M., 2003. Satellite and hydrographic observations of eddy-induced shelf-slope exchange in the northwestern Gulf of Alaska. J. Geophys. Res. Ocn 108 (C2).
- Oliver, E.C., Donat, M.G., Burrows, M.T., Moore, P.J., Smale, D.A., Alexander, L.V., Benthuysen, J.A., Feng, M., Sen Gupta, A., Hobday, A.J., Holbrook, N.J., 2018. Longer and more frequent marine heatwaves over the past century. Nat. Commun. 9 (1), 1–12.
- Overland, J., Rodionov, S., Minobe, S., Bond, N., 2008. North Pacific regime shifts: definitions, issues and recent transitions. Prog. Oceanogr. 77 (2–3), 92–102.
- Reynolds, R.W., Smith, T.M., Liu, C., Chelton, D.B., Casey, K.S., Schlax, M.G., 2007. Daily high-resolution-blended analyses for sea surface temperature. J. Clim. 20 (22), 5473–5496.
- Ross, T., Fisher, J., Bond, N., Galbraith, M., Whitney, F., 2019. The Northeast Pacific: current status and recent trends. PICES Press 27 (1), 36–39.
- Royer, T.C., 1982. Coastal fresh water discharge in the northeast Pacific. J. Geophys. Res. Ocn. 87 (C3), 2017–2021.
- Royer, T.C., 1993. High-latitude oceanic variability associated with the 18.6-year nodal tide. J. Geophys. Res. 98 (C3), 4639–4644.
- Royer, T.C., Emery, W.J., 1987. Circulation in the Gulf of Alaska, 1981. Deep Sea Res. A. 34 (8), 1361–1377.
- Royer, T.C., 1989. Upper ocean temperature variability in the northeast Pacific Ocean: Is it an indicator of global warming? J. Geophys. Res. 94 (C12), 18175–18183.
- Schmeisser, L., Bond, N.A., Siedlecki, S.A., Ackerman, T.P., 2019. The role of clouds and surface heat fluxes in the maintenance of the 2013–2016 Northeast Pacific marine heatwave. J. Geophys. Res. Atmos. 124 (20), 10772–10783.
- Stabeno, P.J., Bell, S., Cheng, W., Danielson, S., Kachel, N.B., Mordy, C.W., 2016. Long-term observations of Alaska coastal current in the northern Gulf of Alaska. Deep Sea Res. II 132, 24–40.
- Stabeno, P.J., Bond, N.A., Hermann, A.J., Kachel, N.B., Mordy, C.W., Overland, J.E., 2004. Meteorology and oceanography of the northern Gulf of Alaska. Continent. Shelf Res. 24 (7–8), 859–897.
- Suryan, R.M., et al., 2021. Ecosystem response persists after a prolonged marine heatwave. Scientific Reports 11 (1), 1–17.
- Swain, D.L., 2015. A tale of two California droughts: lessons amidst record warmth and dryness in a region of complex physical and human geography. Geophys. Res. Lett. 42 (22), 9999-10.
- Taylor, K.E., 2001. Summarizing multiple aspects of model performance in a single diagram. J. Geophys. Res. Atmos. 106 (D7), 7183–7192.
- Walsh, J.E., Thoman, R.L., Bhatt, U.S., Bieniek, P.A., Brettschneider, B., Brubaker, M., Danielson, S., Lader, R., Fetterer, F., Holderied, K., Iken, K., 2018. The high latitude marine heat wave of 2016 and its impacts on Alaska. B. Am. Met. Soc. 99 (1), S39–S43.
- Wei, J.A., Wang, D., Gong, F., He, X., Bai, Y., 2017. The influence of increasing water turbidity on sea surface emissivity. IEEE Trans. Geosci. Rem. Sens. 55 (6), 3501–3515.
- Weingartner, T.J., Coyle, K., Finney, B., Hopcroft, R., Whitledge, T., Brodeur, R., Dagg, M., Farley, E., Haidvogel, D., Royer, T., 2002. The northeast Pacific GLOBEC program: coastal Gulf of Alaska. Oceanography 15 (2).
- Weingartner, T.J., Danielson, S.L., Royer, T.C., 2005. Freshwater variability and predictability in the Alaska coastal current. Deep Sea Res. II 52 (1–2), 169–191.
- Weitzman, B., Konar, B., Iken, K., Coletti, H., Monson, D., Suryan, R., Dean, T., Hondolero, D., Lindeberg, M., 2021. Changes in rocky intertidal community

structure during a marine heatwave in the northern Gulf of Alaska. Front. Mar. Sci. $8,\,556820.$

Wendler, G., et al., 2016. On the climate and climate change of Sitka, Southeast Alaska. Theoretical and Applied Climatology 126 (1), 27–34.

Wilson, J.G., Overland, J.E., 1987. Meteorology. In: Hood, D.W., Zimmerman, S.T.
 (Eds.), The Gulf of Alaska: Physical Environment and Biological Resources. U.S.
 Department of Commerce, Washington D.C, pp. 31–56.
 Wolter, K., Timlin, M.S., 2011. El Niño/Southern Oscillation behaviour since 1871 as

Wolter, K., Timlin, M.S., 2011. El Niño/Southern Oscillation behaviour since 1871 as diagnosed in an extended multivariate ENSO index (MEI.ext). Int. J. Climatol. 31 (7), 1074–1087.